LJMU Research Online

Desai, DD, Ashall, C, Shappee, BJ, Morrell, N, Galbany, L, Burns, CR, Derkacy, JM, Hinkle, JT, Hsiao, E, Kumar, S, Lu, J, Phillips, MM, Shahbandeh, M, Stritzinger, MD, Baron, E, Bersten, MC, Brown, PJ, De Jaeger, T, Elias-Rosa, N, Folatelli, G, Huber, ME, Mazzali, P, Müller-Bravo, TE, Piro, AL, Polin, A, Suntzeff, NB, Anderson, JP, Chambers, KC, Chen, TW, De Boer, T, Fulton, MD, Gao, H, Gromadzki, M, Inserra, C, Magnier, EA, Nicholl, M, Ragosta, F, Wainscoat, R and Young, DR

 Fast and not-so-furious: Case study of the fast and faint Type IIb SN 2021bxu

http://researchonline.ljmu.ac.uk/id/eprint/24447/

Article

For more information please contact researchonline@ljmu.ac.uk

Fast and not-so-furious: Case study of the fast and faint Type IIb SN 2021bxu

Dhvanil D. Desai [,1]* Chris Ashall [,2] Benjamin J. Shappee [,1] Nidia Morrell [,3] Lluís Galbany [,4,5]
Christopher R. Burns,[6] James M. DerKacy [,2] Jason T. Hinkle [,1] Eric Hsiao [,7] Sahana Kumar [,7]
Jing Lu [,7] Mark M. Phillips [,3] Melissa Shahbandeh [,8] Maximilian D. Stritzinger [,9]
Eddie Baron [,10,11] Melina C. Bersten,[12,13,14] Peter J. Brown [,15] Thomas de Jaeger,[1] Nancy Elias-Rosa,[4]
Gastón Folatelli,[12,13,14] Mark E. Huber [,1] Paolo Mazzali,[16] Tomás E. Müller-Bravo [,4,5]
Anthony L. Piro,[6] Abigail Polin,[6] Nicholas B. Suntzeff,[15] Joseph P. Anderson [,17,18]
Kenneth C. Chambers [,1] Ting-Wan Chen [,19,20] Thomas de Boer [,1] Michael D. Fulton [,21] Hua Gao [,1]
Mariusz Gromadzki [,22] Cosimo Inserra [,23] Eugene A. Magnier [,1] Matt Nicholl [,21] Fabio Ragosta [,24]
Richard Wainscoat [1] and David R. Young[21]

Affiliations are listed at the end of the paper

ABSTRACT

We present photometric and spectroscopic observations and analysis of SN 2021bxu (ATLAS21dov), a low-luminosity, fast-evolving Type IIb supernova (SN). SN 2021bxu is unique, showing a large initial decline in brightness followed by a short plateau phase. With $M_r = -15.93 \pm 0.16$ mag during the plateau, it is at the lower end of the luminosity distribution of stripped-envelope supernovae (SE-SNe) and shows a distinct $\sim$10 d plateau not caused by H- or He-recombination. SN 2021bxu shows line velocities which are at least $\sim 1500 \, \mathrm{km \, s^{-1}}$ slower than typical SE-SNe. It is photometrically and spectroscopically similar to Type IIb SNe during the photospheric phases of evolution, with similarities to Ca-rich IIb SNe. We find that the bolometric light curve is best described by a composite model of shock interaction between the ejecta and an envelope of extended material, combined with a typical SN IIb powered by the radioactive decay of ^{56}Ni. The best-fitting parameters for SN 2021bxu include a ^{56}Ni mass of $M_{\mathrm{Ni}} = 0.029^{+0.004}_{-0.005} \, \mathrm{M_\odot}$, an ejecta mass of $M_{\mathrm{ej}} = 0.61^{+0.06}_{-0.05} \, \mathrm{M_\odot}$, and an ejecta kinetic energy of $K_{\mathrm{ej}} = 8.8^{+1.1}_{-1.0} \times 10^{49}$ erg. From the fits to the properties of the extended material of Ca-rich IIb SNe we find a trend of decreasing envelope radius with increasing envelope mass. SN 2021bxu has M_{Ni} on the low end compared to SE-SNe and Ca-rich SNe in the literature, demonstrating that SN 2021bxu-like events are rare explosions in extreme areas of parameter space. The progenitor of SN 2021bxu is likely a low-mass He star with an extended envelope.

Key words: stars: massive – supernovae: general – supernovae: individual: SN 2021bxu.

1 INTRODUCTION

Core-collapse (CC) supernovae (SNe) mark the explosive ends of the lives of massive stars ($M \gtrsim 8 \, \mathrm{M_\odot}$) via gravitational collapse of their stellar cores. Some CC SNe occur from progenitors that have lost their outer envelopes and are classified as stripped-envelope supernovae (SE-SNe; Clocchiatti et al. 1996; Matheson et al. 2001). Optical spectral signatures of H and He are mainly used to distinguish between the different types of SE-SNe (Filippenko 1997). The lack of H and Si II λ6150 features defines Type Ib/c SE-SNe. Furthermore, if there is He I λ5876 absorption present, the SN is a Type Ib and if there is weak or no He I λ5876 absorption, the SN is a Type Ic. In addition to these types, SNe that show transient lines of H, making

their late-time spectra appear more like SNe Ib, are classified as Type IIb SNe.

The exact nature of progenitor scenarios is unclear but different types of SE-SNe may be explained by various mass-loss mechanisms in the progenitor star (Filippenko, Matheson & Barth 1994). SNe Ic likely result from stars that have lost both their H and He envelopes, SNe Ib from stars with less extreme stripping that have lost H envelope, and SNe IIb result from stars that have lost most of their H envelope, showing weak H lines at early times (e.g. Filippenko 1997; Prentice & Mazzali 2017; Shivvers et al. 2017). It is unclear if there is a continuum between each type of SE-SN or whether this points towards multiple mass-loss mechanisms. Some common proposed mass-loss mechanisms which may be responsible for stripping the stellar envelope(s) include (a) outbursts in Luminous Blue Variables (e.g. Smith & Owocki 2006), (b) radiation-driven winds (e.g. Heger et al. 2003; Pauldrach, Vanbeveren & Hoffmann 2012), (c) envelope stripping due to close binary interactions (e.g. Podsiadlowski et al.

1993, 2004; Woosley, Langer & Weaver 1995; Wellstein & Langer 1999; Wellstein, Langer & Braun 2001; Benvenuto, Bersten & Nomoto 2013), (d) mass-loss in rapidly rotating Be stars (e.g. Massa 1975; Kogure & Hirata 1982; Owocki 2006), or a combination of these.

The low-mass end of SE-SN progenitors [zero-age main-sequence (ZAMS) mass ~ 8–$12\,M_\odot$] is not well understood (e.g. Janka 2012). However, it is known that stars in this mass range could end their evolution as white dwarfs (WDs), explode as low-luminosity electron-capture SNe, or ignite nuclear burning leading to 'standard' iron CC explosions (e.g. Miyaji et al. 1980; Hillebrandt, Nomoto & Wolff 1984; Nomoto 1984; Miyaji & Nomoto 1987; Nomoto 1987; Heger et al. 2003). Their end stages of evolution depend strongly on composition, metallicity, mass-loss history, etc. (e.g. Poelarends et al. 2008, and references therein). In the case of SN explosions from progenitors with M_{ZAMS} in the range ~ 8–$12\,M_\odot$, it is possible to observe (a) relatively faint Type II SNe (IIP or IIL depending on the mass of the H-rich envelope) with presumably low degree of interaction, (b) Type IIb SNe having a stronger interaction with a circumstellar material, or (c) SE-SNe (e.g. Pumo et al. 2009, and references therein). Given a stellar initial mass function (IMF) that drops steeply towards higher masses, we should expect a significant fraction of CC SNe to have lower mass progenitors (e.g. Sukhbold et al. 2016). However, due to their expected lower luminosities and rapid photometric evolution, SNe resulting from low-mass stars are likely more difficult to observe and follow-up, leading to an observational bias (Nomoto et al. 1982; Janka 2012).

Recently, Calcium-rich transients have emerged as a new class of SNe showing faster photometric evolution than normal SNe, lower luminosities, and a nebular phase dominated by calcium emission (Perets et al. 2011; Kasliwal et al. 2012; Shen, Quataert & Pakmor 2019; Das et al. 2022). Ca-rich transients consist of two main sub-types: I and II. The Type I Ca-rich transients may come from the explosion of WDs or highly stripped CC events (Kawabata et al. 2010; Tauris, Langer & Podsiadlowski 2015). They do not show hydrogen in their spectra and are usually found in the outskirts of early-type galaxies, in old, metal-poor environments (Perets et al. 2011). The Type II Ca-rich transients, which possibly come from a CC event, show hydrogen features. In particular, Ca-rich Type IIb have spectra similar to SNe IIb near peak light, but rapidly evolve into nebular phase ($\sim$30 d after explosion) and show a [Ca II]/[O I] ratio of ≥ 2 (Das et al. 2022). Contrary to the Ca-rich Type I transients, Ca-rich Type IIb SNe are found in star-forming regions and suggest a new class of strongly stripped SNe (SS-SNe) which have ejecta masses less than $\sim 1\,M_\odot$ and stripped low-mass He stars as their progenitors.

One of the most promising ways to study the progenitor and its outermost layers is through early-time observations of SN explosions (e.g. Bersten et al. 2012; Piro & Nakar 2013; Vallely et al. 2021). Shock-breakout is an early-time phenomenon that occurs on a time-scale of a few minutes to hours when the shock from a CC explosion of a massive star breaks through the stellar surface (Waxman & Katz 2017). For CC events, shock-breakout is a promising tool for measuring the properties of the exploding star through early-time observations of the outer layers. This manifests as X-ray and ultraviolet (UV) brightening, followed by a post-shock breakout cooling phase where most of the radiation is emitted in UV and optical and the envelope expands while cooling down. The time-scale of this phenomenon depends on the type of progenitor and the presence or absence of extended material around the star. For example, for normal SNe Ib or Ic this lasts a few hours (e.g. Xiang et al. 2019) and for SNe IIb with extended envelopes this is of the

order of a few days (e.g. Nomoto et al. 1993). Since the shock-breakout and cooling depend on properties of the outermost layers of the progenitor, observing those via early-time observations can provide measurements of the temperature, radius, and mass of the envelope or circumstellar material (e.g. Nakar & Piro 2014; Piro, Haynie & Yao 2021).

Few SE-SNe have been observed to exhibit so-called 'double-peaked' light curves with an initial decline due to shock cooling and a second peak due to the radioactive decay of ^{56}Ni, which normally powers the light curve. Generally, these objects were classified as SNe IIb. The first of this class was the well-studied SN 1993J (Richmond et al. 1994), followed by other SE-SNe, e.g. SN 2011dh (Arcavi et al. 2011), SN 2011fu (Morales-Garoffolo et al. 2015), SN 2013df (Morales-Garoffolo et al. 2014), and some others as shown in Prentice et al. (2020). The initial decline in SN 1993J was explained as a result of a lengthened shock cooling due to the shock passing through an extended envelope around the star instead of 'breaking out' at an abrupt surface, producing a longer initial decline. Similar to that observed in various SNe IIb, a subset of Ca-rich transients have also been shown to have double-peaked light curves with an initial decline of a few days that are well fit by an extended envelope model (Das et al. 2022). For example, Ertini et al. (in preparation) showed that SN 2021gno, a Ca-rich SN Ib with double-peaked light curves, can be well modelled by a CC explosion of a highly stripped, massive star.

Exotic classes of SNe are being discovered by untargeted surveys such as the All-Sky Automated Survey for SuperNovae (ASAS-SN; Shappee et al. 2014; Kochanek et al. 2017), the Asteroid Terrestrial-impact Last Alert System (ATLAS; Tonry et al. 2018; Smith et al. 2020), and the Zwicky Transient Facility (ZTF; Bellm et al. 2019; Masci et al. 2019), and studied with high-precision multiband early follow-up by programs such as the Precision Observations of Infant Supernova Explosions (POISE; Burns et al. 2021) collaboration. SN 2021csp (Fraser et al. 2021), SN 2021fxy (DerKacy et al. 2023), SN 2021gno (Ertini et al. in preparation), and SN 2021aefx (Ashall et al. 2022) are all SNe followed up by POISE, and each of them demonstrates the power of obtaining high-precision early-time observations by providing insight into their sub-class of SNe.

In this work, we study SN 2021bxu[1] (ATLAS21dov), a peculiar SE-SN discovered by ATLAS on UT 2021 February 06.3 (Tonry et al. 2021) and later classified as a Type IIb SN (DerKacy 2021). Early-time observations from POISE show a fast-declining light curve followed by a $\sim$10 d plateau and an unusually low peak luminosity. Here, we present a detailed study of this unique event with high-precision photometry and spectroscopy, explore a new parameter space for SNe and their progenitors, and derive physical quantities and compare them with other known SE-SNe.

In Section 2, we provide the properties of the host galaxy. In Section 3, we describe the photometric and spectroscopic observations of SN 2021bxu. In Section 4, we analyse and compare the multiband light curves and colour curves of SN 2021bxu with SE-SNe and Ca-rich IIb SNe from literature. We also derive and compare the pseudo-bolometric and bolometric light curves of SN 2021bxu with a sample of SE-SNe. In Section 5, we identify the observed spectroscopic lines, compare the line velocities to a sample of SE-SNe and Ca-rich IIb SNe, estimate the time of explosion, and compare SN 2021bxu with similar SNe. In Section 6, we outline the models used to fit the bolometric and pseudo-bolometric light curves, describe the fitting method and present the best-fitting results for the

---

[1] https://www.wis-tns.org/object/2021bxu

Table 1. Global and local properties of the host galaxy ESO 478- G 006.

	Global (phot)	Local (spec)
Age [yr]	$2.2^{+8.5}_{-1.2} \times 10^8$	$9^{+11}_{-8} \times 10^8$
M_* [$M_\odot$]	$2.3^{+1.3}_{-0.6} \times 10^{10}$	$(3.2 \pm 0.2) \times 10^6$
SFR [$M_\odot$ yr^{-1}]	34^{+16}_{-27}	$(7.38 \pm 0.09) \times 10^{-5}$
sSFR [yr^{-1}]	$1.5^{+1.2}_{-1.3} \times 10^{-9}$	$2.3^{+1.2}_{-0.4} \times 10^{-11}$
$A_{V,\mathrm{host}}$ [mag]	$1.4^{+0.2}_{-0.9}$	0.4 ± 0.2
$12 + \log_{10}(\mathrm{O/H})$	–	8.71 ± 0.14
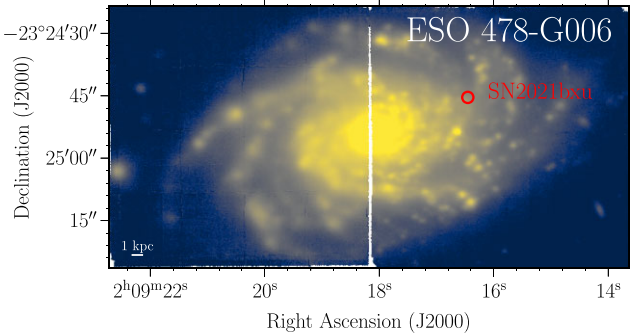
Figure 1. Finding chart of SN 2021bxu in its host galaxy ESO 478- G 006 obtained with MUSE. The background image is a stellar-continuum-subtracted Hα emission map obtained from the two MUSE pointings. The different conditions of the observations are evident, the west half of the galaxy where SN 2021bxu exploded presents a better spatial resolution (0.72 arcsec seeing) than the east half (2.01 arcsec seeing).

explosion parameters. In Section 7, we compare and contextualize the physical parameters of SN 2021bxu with a sample of SE-SNe and Ca-rich IIb SNe. Finally, in Section 8, we summarize our work and present the conclusions.

2 HOST GALAXY PROPERTIES

The host galaxy ESO 478- G 006 is classified as an Sbc galaxy with luminosity class II–III (de Vaucouleurs et al. 1991). SN 2021bxu was discovered in one of the spiral arms of its host galaxy.

Using the Fitting and Assessment of Synthetic Templates (FAST; Kriek et al. 2009), we fit stellar population synthesis models to the archival photometry (see Table A3 in Appendix A) of the host galaxy ESO 478- G 006 to obtain the global age, the total stellar mass, the star formation rate (SFR), and the specific SFR (sSFR). These global parameters are reported in Table 1 as best-fitting values with uncertainties from Monte Carlo. Our fit assumes a Cardelli, Clayton & Mathis (1989) extinction law with $R_V = 3.1$, a Salpeter IMF (Salpeter 1955), an exponentially declining SFR, the Bruzual & Charlot (2003) stellar population models, and allows for a variable average host galaxy extinction higher than the Galactic foreground value of $A_{V,\mathrm{MW}} = 0.045$ mag. The value of host extinction from this fit indicates an average across the entire galaxy and is not necessarily the value at the site of the SN.

To estimate the local host extinction and other properties, we used integral field spectroscopy (IFS) obtained with MUSE mounted to the 8.2m Very Large Telescope (VLT) in 2016 October as a part of the All-weather MUse Supernova Integral-field of Nearby Galaxies (AMUSING; Galbany et al. 2016; López-Cobá et al. 2020) survey. Two pointings were observed covering the position of SN 2021bxu (see Fig. 1). Following previous analysis of IFS data (e.g. Galbany et al. 2014, 2018), we extracted a 2 arcsec aperture spectrum from the

IFS cube centred at the SN location, and performed spectral synthesis with STARLIGHT (Cid Fernandes et al. 2005). By subtracting the best STARLIGHT fit from the observed spectrum, we get the gas-phase spectrum, where we fit Gaussian profiles to the strongest emission lines to measure the main properties of the ionized gas. In particular, the dust extinction along the line of sight is estimated using the colour excess ($E(B - V)$) from the ratio of the Balmer lines, assuming an intrinsic ratio $I(\mathrm{H}\alpha)/I(\mathrm{H}\beta) = 2.86$, valid for case B recombination with $T = 10,000$ K and electron density 10^2 cm^{-3} (Osterbrock & Ferland 2006), and using a Cardelli et al. (1989) extinction law. Local properties are also listed in Table 1.

For the purposes of magnitude corrections for SN 2021bxu, we use a null line-of-sight host extinction at the SN site, as inferred from the absence of strong narrow Na I D line in the SN spectra. We do not use $A_{V,\mathrm{host}} = 0.4 \pm 0.2$ mag from local spectroscopic analysis of the host galaxy because this measurement is of the extinction from the total line-of-sight dust column. Since we do not know if the SN exploded in front of the dust column or behind it, using the galaxy measurement is not optimal. However, we note that there may be up to 0.4 mag of host extinction and including this in the analysis does not change the conclusions of this study.

3 DATA

3.1 Photometry

We present high-precision multiband photometry of SN 2021bxu obtained with the Henrietta Swope 1.0 m telescope at Las Campanas Observatory, ASAS-SN, ATLAS, and the Panoramic Survey Telescope and Rapid Response System (Pan-STARRS; Chambers et al. 2016; Flewelling et al. 2020, see table A1 in Appendix A).

The Swope photometry, in *BVugri* bands, was produced using custom reduction and calibration procedures as described in Krisciunas et al. (2017) and Phillips et al. (2019) via the POISE collaboration, which builds on the legacy of the Carnegie Supernova Project (CSP; Phillips et al. 2019). The science images were host-galaxy template subtracted and the nightly zero-points were obtained on photometric nights by observing photometric standards from the Landolt (1992) and Smith et al. (2002) catalogues. Using these zero-points, we computed natural magnitudes of the local sequence stars (listed in Table A2 in Appendix A) in the field, which is then used to calibrate the Swope photometry of SN 2021bxu. The Swope photometry is ultimately in the CSP natural system. The ATLAS photometry, in *o* and *c* bands, was obtained from the ATLAS Forced Photometry server[2] (Shingles et al. 2021), with photometry produced as outlined in Tonry et al. (2018) and Smith et al. (2020). The ASAS-SN *g*-band light curve was produced using subtracted aperture photometry from ASAS-SN Sky Patrol.[3] Finally, the Pan-STARRS (PS) observations were taken with both 1.8 m telescope units located at the summit of Haleakala (Chambers et al. 2016), in an SDSS-like filter system, denoted as *grizy*$_{\mathrm{PS}}$, and a broad *w*$_{\mathrm{PS}}$ filter, which is a composite of the *gri*$_{\mathrm{PS}}$ filters. Pan-STARRS data are processed in real time as described in Magnier et al. (2020a, b) and Waters et al. (2020). The data are subject to difference imaging with the Pan-STARRS1 3π sky survey data (Chambers et al. 2016) used as references, and photometric zero-points on the target images were set with field stars from the Pan-STARRS1 3π catalogue (Flewelling et al. 2020).

[2] https://fallingstar-data.com/forcedphot/
[3] https://asas-sn.osu.edu/

MJD [days]
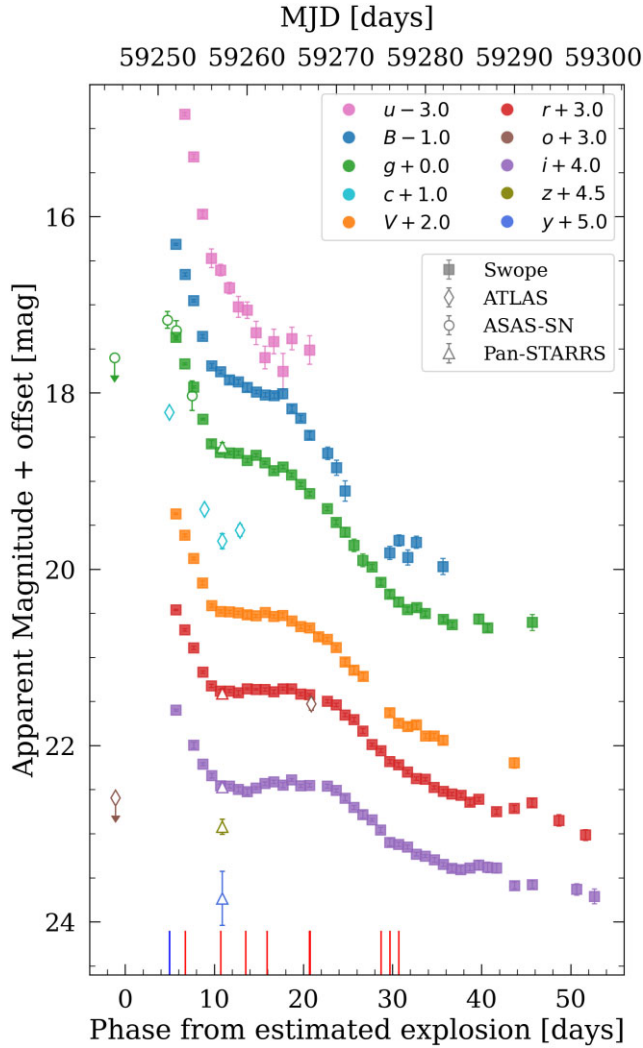
Figure 2. Multiband light curves of SN 2021bxu from Swope *BVugri*, ATLAS *oc*, ASAS-SN *g*, and Pan-STARRS *grizy*. Non-detections in ASAS-SN *g* and ATLAS *o* are shown as points with downward-facing arrows. The vertical red line segments at the bottom of the plot mark the epochs of spectroscopic observations and the blue line segment marks the discovery. The estimated time of explosion is further explained in Section 4.3.

All light curves from Swope, ATLAS, ASAS-SN, and Pan-STARRS are shown in Fig. 2. The Pan-STARRS *w* band has a non-detection with a 5σ upper limit of $m_{w_{PS}} > 22.3$ mag 33 d before discovery showing no previous outbursts and an upper limit of $m_{w_{PS}} > 21.7$ mag 216 d after the last measurement from Swope. The ATLAS *o* band has a non-detection with a 5σ upper limit of $m_o > 19.6$ mag 6.02 d before discovery and an upper limit of $m_o > 19.8$ mag 101 d after the last measurement from Swope. ASAS-SN also has a non-detection with a 5σ upper limit of $m_g > 17.6$ mag 6.16 d before discovery along with the first detection at a maximum of $m_g = 17.17 \pm 0.09$ mag 0.2 d before discovery. The non-detection and the first detection can help constrain the time of explosion (see Section 5.3).

We obtained UV observations from the Ultra-Violet Optical Telescope (UVOT; Roming et al. 2005) on the *Neil Gehrels Swift Observatory* (Gehrels et al. 2004) about 20 d after the estimated explosion but did not detect the SN. Pre-explosion imaging from 2018 and 2019 is available in the *U* and *UVW*1 filters because of the Swift

Table 2. Properties of SN 2021bxu.

RA (J2000)	02:09:16.47
δ (J2000)	-23:24:45.15
z [a]	0.0178
Host galaxy	ESO 478- G 006
Host offset [b]	9.2 ± 0.6 kpc
$E(B-V)_{MW}$ [c]	0.014 mag
$E(B-V)_{Host}$	~ 0 mag
μ [a]	34.28 ± 0.16 mag
D_L [d]	72 ± 5 Mpc
Last Non-Detection (MJD)	59245.12 d
Discovery (MJD)	59251.28 d
Estimated Explosion (MJD) [e]	59246.3 ± 0.4 d

Notes. [a]Scolnic et al. (2018).
[b]Projected offset from the host-galaxy nucleus.
[c] Schlafly & Finkbeiner (2011).
[d]Computed using μ from Scolnic et al. (2018).
[e]See Section 5.3.

Gravitational Wave Galaxy Survey, the intent of which is to obtain galaxy template images before the detection of transients (Klingler et al. 2019). Using the pipeline from the Swift Optical Ultraviolet Supernova Archive (SOUSA; Brown et al. 2014), we measure upper limits on MJD 59266.3 of $UVW1 > 19.1$ mag and $U > 19.1$ mag. These magnitude limits are in the UVOT/Vega system using zero-points from Breeveld et al. (2011), the time-dependent sensitivity correction from 2020 September,[4] and an aperture correction updated in 2022. Subsequent observations over the next 10 d yield similar limits and are available from the SOUSA.

There are no data from ZTF or the Transiting Exoplanet Survey Satellite (TESS; Ricker et al. 2016; Fausnaugh et al. 2021; Fausnaugh et al., in preparation) for this object during the time period of interest.

To convert from apparent to absolute magnitudes we need the distance modulus and extinction corrections. The distance modulus for SN 2021bxu ($\mu = 34.28 \pm 0.16$ mag) is measured using precise redshift-independent distance measurement using the Type Ia SN 2009le that exploded in the host galaxy (ESO 478- G 006; Scolnic et al. 2018). We infer no host-galaxy extinction at the site of the SN due to a lack of narrow Na I D lines in the SN spectra (Phillips et al. 2013). Therefore, using μ and the Galactic extinction correction ($E(B-V)_{MW} = 0.014$ mag; Schlafly & Finkbeiner 2011), we obtain the absolute magnitudes listed in Table A1. Some of the properties of SN 2021bxu are listed in Table 2 and the photometric analysis is further discussed in Section 4.

3.2 Spectroscopy

Along with the photometry, we also have a total of 10 spectroscopic observations for SN 2021bxu. These include optical spectra with spectral range of roughly 4000–9000 Å obtained from the Dual Imaging Spectrograph (DIS) on the Apache Point Observatory (APO), the ESO Faint Object Spectrograph and Camera v.2 (EFOSC2; Buzzoni et al. 1984) on the New Technology Telescope (NTT), the Alhambra Faint Object Spectrograph and Camera (ALFOSC) on the Nordic Optical Telescope (NOT), the Gemini Multi-Object Spectrograph (GMOS; Hook et al. 2004) on the Gemini North telescope, and the Inamori-Magellan Areal Camera and Spectrograph (IMACS; Dressler et al. 2011) on the Magellan Baade telescope. The

---

[4]https://heasarc.gsfc.nasa.gov/docs/heasarc/caldb/swift/docs/uvot/uvotcaldb_throughput_06.pdf

Table 3. Spectroscopy of SN 2021bxu.

Date (UT)	MJD (d)	Phase[a] (d)	Telescope	Instrument
2021 Feb 8	59253.07	6.7	APO	DIS
2021 Feb 12	59257.02	10.7	NTT	EFOSC2
2021 Feb 14	59259.84	13.5	NOT	ALFOSC
2021 Feb 17	59262.22	15.9	Gemini	GMOS-N
2021 Feb 22	59267.01	20.7	NTT	EFOSC2
2021 Feb 22	59267.04	20.7	NTT	EFOSC2
2021 Feb 22	59267.05	20.7	Baade	IMACS
2021 Mar 2	59275.04	28.7	Baade	IMACS
2021 Mar 3	59276.01	29.7	NTT	EFOSC2
2021 Mar 4	59277.00	30.7	NTT	EFOSC2

Note. [a]From estimated explosion date (MJD 59246.3) in rest frame.

spectra from APO and Baade were reduced using standard IRAF[5] packages with the methods as described in Hamuy et al. (2006) and Folatelli et al. (2013). The NOT data were taken as a part of the NUTS2 collaboration[6] and reduced using the FOSCGUI pipeline[7] The NTT spectra were obtained through the Public European Southern Observatory Spectroscopic Survey of Transient Objects (PESSTO) program, and reduced using the data reduction pipeline described in Smartt et al. (2015). The Gemini spectra were reduced using a custom-made IRAF routine. Dates and phases of all spectra are listed in Table 3.

Fig. 3 shows the spectral sequence. The original unbinned spectra are in grey and the higher signal-to-noise ratio (SNR), binned spectra are in colours. The unbinned spectra are resampled at a resolution of 10 Å using SpectRes (Carnall 2017) to produce the binned spectra. The two NTT spectra on UT 2021 February 22 are taken only one half-hour apart and, since they are on the same telescope and instrument, we average them to produce a combined spectrum with a higher SNR. This combined spectrum is used for all following analysis.

4 PHOTOMETRIC ANALYSES

4.1 Multiband light curves

The multiband light curves of SN 2021bxu are presented in Fig. 2, ranging from the *u* band to the *i* band. There is a decrease of ~1.7 mag in the *u* band from ~17.9 to ~19.5 mag in the first 3 d and thereafter it keeps decreasing almost linearly, but with a shallower slope. However, moving to the optical bands, a plateau starts appearing, which becomes more prominent in the redder bands. For example, in the *g* band, the brightness declines by ~1.5 mag in the first ~5 d after discovery and it is followed by a plateau where the brightness stays roughly constant for the next ~10 d before declining again. Looking at the *i* band, where it gets moderately bright again, this plateau may be interpreted as a second peak. Using the distance

---

[5]The Image Reduction and Analysis Facility (IRAF) is distributed by the National Optical Astronomy Observatory, which is operated by the Association of Universities for Research in Astronomy, Inc., under cooperative agreement with the National Science Foundation.

[6]https://nuts.sn.ie/

[7]FOSCGUI is a Python-based graphic user interface developed by E. Cappellaro and aimed at extracting SN spectroscopy and photometry obtained with FOSC-like instruments. A package description can be found at https://sngroup.oapd.inaf.it/foscgui.html

modulus $\mu = 34.28 \pm 0.16$ mag from Table 2, we obtain a peak *r*-band magnitude of $M_r = -16.86 \pm 0.16$ mag at the first epoch. After the initial decline, the absolute magnitude during the plateau phase is $M_r = -15.93 \pm 0.16$ mag as estimated from the ^{56}Ni peak (see Section 6).

In Fig. 4, we show the light curves of SN 2021bxu in *BVugri* bands normalized to the bolometric ^{56}Ni peak (discussed in Section 6) in each band along with a sample of various types of SE-SNe (IIb, Ib, and Ic) from Stritzinger et al. (2018a), a sample of SNe II from Anderson et al. (2014), and a sample of Ca-rich Type IIb SNe from Das et al. (2022). The most obvious distinction between SN 2021bxu and the rest of the sample is the presence of a strong initial decline in brightness. Although dissimilar to most SNe II having the typical long plateau phase, SN 2021bxu shows similarities to the light curves of Type II-L SN 2001fa and SN 2007fz (Faran et al. 2014) including an initial decline and rise to a second peak. However, SN 2021bxu has much less H in the spectra than the two SNe II-L. SN 2001fa and SN 2007fz have been proposed as a link between SNe II and SNe IIb because of the intermediate strength H α P-Cygni profile between those SN Types. Nevertheless, Pessi et al. (2019) find no evidence of continuum between SNe II and SNe IIb. On the other hand, the overall shape of SN 2021bxu's later decline matches well with the SE-SNe and especially well with the Ca-rich IIb SNe and with SNe IIb. The Ca-rich IIb SNe show a wide range of initial declines depending on the properties of the external layers of the progenitor (Das et al. 2022). However, the later decline in the *g* band for SN 2021bxu is almost identical to that of the Ca-rich IIb and SNe IIb samples.

4.2 Colour curves

With the available multiband photometry, we produce the Milky Way reddening-corrected $B - V$, $u - g$, $g - r$, and $r - i$ colour curves for SN 2021bxu, presented in Fig. 5. The $u - g$ colour quickly reaches a reddest value of ~1.7 mag ~15 d after explosion. The $B - V$ and $g - r$ colours follow a trend similar to each other and get to their reddest value of ~1.1 mag ~25 d after explosion. The $B - V$ colour shows an unexpected change of slope around ~16–19 d after explosion corresponding to the time of the plateau phase. On the other hand, starting off at the bluest colour, the $r - i$ colour shows a slow but steady increase from ~−0.1 to ~0.3 mag over the ~40 d after explosion.

We compare the colour curves of SN 2021bxu to templates from Stritzinger et al. (2018b) for SE-SNe Ib, Ic, and IIb as well as SNe II. Fig. 5 shows the colour curves of SN 2021bxu together with the templates. The $B - V$ colour of SN 2021bxu is consistent with SNe Ib until ~5 d after *B*-band maximum but it is bluer by ~0.4 mag around Day 12. The $u - g$ colour follows SNe Ib up to ~5 d after *g*-band maximum, but resembles SNe IIb thereafter. On the other hand, the $g - r$ colour does not seem to match any of the types except the first ~3 d where it matches with SNe II; it is too blue for SE-SNe and too red for SNe II after that. The $B - V$ and the $g - r$ colours peak ~10 d after the templates peak, although the templates only go up to 20 d past maximum. Finally, the $r - i$ colour matches the trend of SNe IIb given the error bars on the data and the model. Although SN 2021bxu shows a plateau in its light curve, the colour curves do not match those of SNe II.

4.3 Bolometric light curves

Our multiband photometry is used to determine the properties of the SN such as its luminosity, radius, and photospheric temperature

Figure 3. Spectra of SN 2021bxu from APO (green), NTT (red), NOT (orange), Gemini (blue), and Baade (purple) from +6.74 to +30.68 d after its estimated explosion (MJD 59246.3), all listed in Table 3. The spectrum from NTT at +20.7 d is an average of two spectra taken on the same night using the same instrument only half-hour apart.

evolution. We construct the bolometric light curve for SN 2021bxu using the multiband photometry in the Swope *BVugri* bands after converting magnitudes to monochromatic fluxes, correcting for the Milky-Way extinction of $E(B - V)_{\mathrm{MW}} = 0.014$ mag, and using the distance of $D_{\mathrm{L}} = 72 \pm 5$ Mpc from Table 2. We use the magnitude offsets and filter profiles from the CSP webpage.[8] If a certain band lacked observations on a given epoch, we interpolated using Gaussian Processes with the `scikit-learn` (Pedregosa et al. 2011) Python library. We fit each epoch's spectral energy distribution (SED) with a Planck blackbody function. The bolometric

luminosity is computed by directly integrating the flux density into the available bands and using the blackbody fits to extrapolate to the unobserved wavelengths. The effective photospheric temperature is the best-fitting temperature from the blackbody fits, and the radius is then computed from luminosity and temperature using the Stefan–Boltzmann law. The errors on luminosity, temperature, and radius are derived from a Monte Carlo procedure using the errors of the original photometry. Photometric precision is high with errors < 1 per cent which means majority of the systematic errors come from the uncertainty in the distance estimate and the assumption of a blackbody SED. The uncertainty in the distance corresponds to a fractional uncertainty in luminosity of $L_{-16\ \mathrm{per\ cent}}^{+13\ \mathrm{per\ cent}}$, which would cause the light curve to shift up or down systematically.
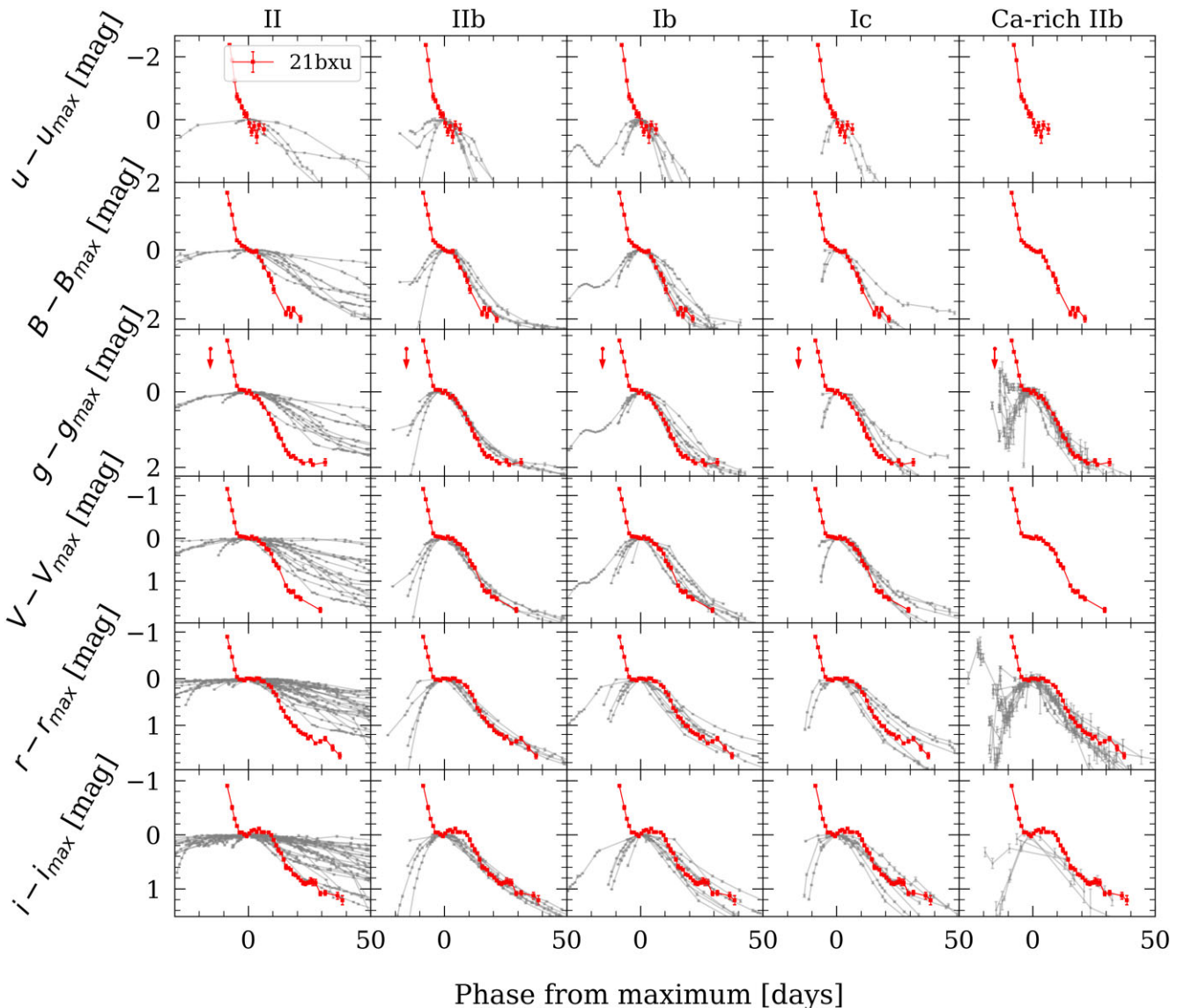
Figure 4. The grey light curves show SNe II, IIb, Ib, and Ic from the CSP (Anderson et al. 2014; Stritzinger et al. 2018a) and Ca-rich Type IIb SNe from Das et al. (2022). The red light curves in each subplot are SN 2021bxu. The *g*-band panel shows the last non-detection from ASAS-SN as the downward-pointing arrow. The epoch of maximum light for normalization is chosen as the peak of the ^{56}Ni component of the light curve (see Section 6).

Fig. 6 shows the bolometric luminosity, temperature, and radius evolution.

The bolometric luminosity starts at $L_{bol} \sim 3.5 \times 10^{42}$ erg s^{-1} at discovery, drops down to $L_{bol} \sim 6.6 \times 10^{41}$ erg s^{-1} during the initial decline, stays flat at that value for $\sim$10 d defining a plateau, and then declines again. The radius increases almost linearly with time initially until $\sim$25 d past explosion, indicating that the black-body extrapolation is reasonable and the black-body radius roughly follows the photospheric radius. At later times, the black-body radius starts declining, although this may lack physical meaning since the black-body approximation is not good at these times.

The photospheric temperature drops from 13 500 to 7000 K during the initial photometric decline, suggesting a rapid cooling of the ejecta, and steadily declines thereafter. Martinez et al. (2022) show that SNe II have a roughly constant temperature evolution during their plateau at $\sim$6000 K due to H-recombination. The temperature evolution of SN 2021bxu during the plateau is not constant; it

decreases from $\sim$7000 to $\sim$5000 K. Combined with the lack of Hα emission, this suggests that H-recombination is likely not responsible for the observed plateau in the light curve, unlike SNe II.

Pseudo-bolometric light curves are used for a direct comparison to similar SNe. Instead of the full wavelength range, pseudo-bolometric light curves are defined only within a finite range usually covering the wavelengths of the observed bandpasses used. We compute the pseudo-bolometric light curve by integrating the fluxes in the range 4000–10 000 Å and compare it with a sample from Prentice et al. (2020) and SN 2021gno (Ertini et al. in preparation), due to their potential similarities in the light curve shape, as seen in Fig. 7. The slope of the initial decline is similar to that of SN 1993J and SN 2021gno; however, they both have a distinct second peak, whereas SN 2021bxu shows a plateau. SN 2021gno has the lowest luminosity with rapid photometric evolution and low explosion energy, ^{56}Ni mass and ejecta mass, characteristic of Ca-rich SNe (Ertini et al.

Figure 5. Colour curves of SN 2021bxu using Swope photometry compared to the Type Ib, Ic, and IIb colour curve templates from CSP SE-SNe sample. We create a template for $B - V$ colour of a Type II SN using SN 2014G (Bose et al. 2016) and for $g - r$ and $r - i$ colours of a Type II SN using DES15E1iuh (de Jaeger et al. 2020). There were no u-band data available for Type II SNe, so we do not have a Type II template for the $u - g$ colour. We do not plot colour curves for Ca-rich IIb SNe due to the lack of a statistical sample or a representative SN.
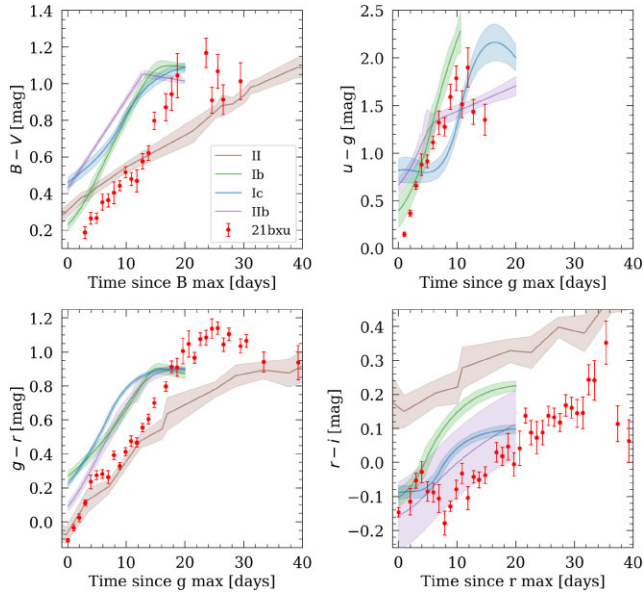
in preparation). We note again that SN 2021bxu is unique due to its low peak luminosity at $\log(L_{\mathrm{pseudo}}/\mathrm{erg\,s^{-1}}) = 42.0$ and a distinct plateau phase at $\log(L_{\mathrm{pseudo}}/\mathrm{erg\,s^{-1}}) \sim 41.6$ from ~ 10 to ~ 20 d post-explosion. This plateau is possibly due to an underlying secondary peak from the radioactive decay of ^{56}Ni similar to SN 1993J and SN 2021gno (further discussed in Sections 6 and 7).

5 SPECTROSCOPIC ANALYSIS

5.1 Line IDs

Due to the homologous expansion of the ejecta, measuring line velocities as a function of time allows us to examine the chemical composition of the ejecta, and understand the structure and the mixing within the explosion. We identify the lines by comparing the spectral features to literature and cross-checking with measured velocities (Section 5.2). There is a total of 10 optical spectra ranging from 7 to 31 d after estimated time from explosion. This allows us to explore the velocity evolution of the absorption features.

The main absorption features are labelled in the spectra shown in Fig. 3. We identify strong absorption features from He I λ5876 and He I λ6678 along with weaker hydrogen Balmer series (Hα λ6563, Hβ λ4861, and Hγ λ4340). The presence of strong helium with some hydrogen is characteristic of a Type IIb SN and confirms the typing of SN 2021bxu as Type IIb. Absorption features from heavier elements such as O I λ7774, Si II $\lambda\lambda$4130, 5972, 6355, Ca II H&K $\lambda\lambda$3934, 3969, IR-triplet $\lambda\lambda$8498, 8542, 8662, and a forest of Fe II lines including the strong Fe II λ5169, are also present. We also identify absorption features from neutron capture elements such as Sc II $\lambda\lambda$5527, 5698, 6280, and Ba II λ6142 in SN 2021bxu. Disentangling whether these are r- or s-process elements is beyond the scope of this study. Interestingly, the neutron capture elements
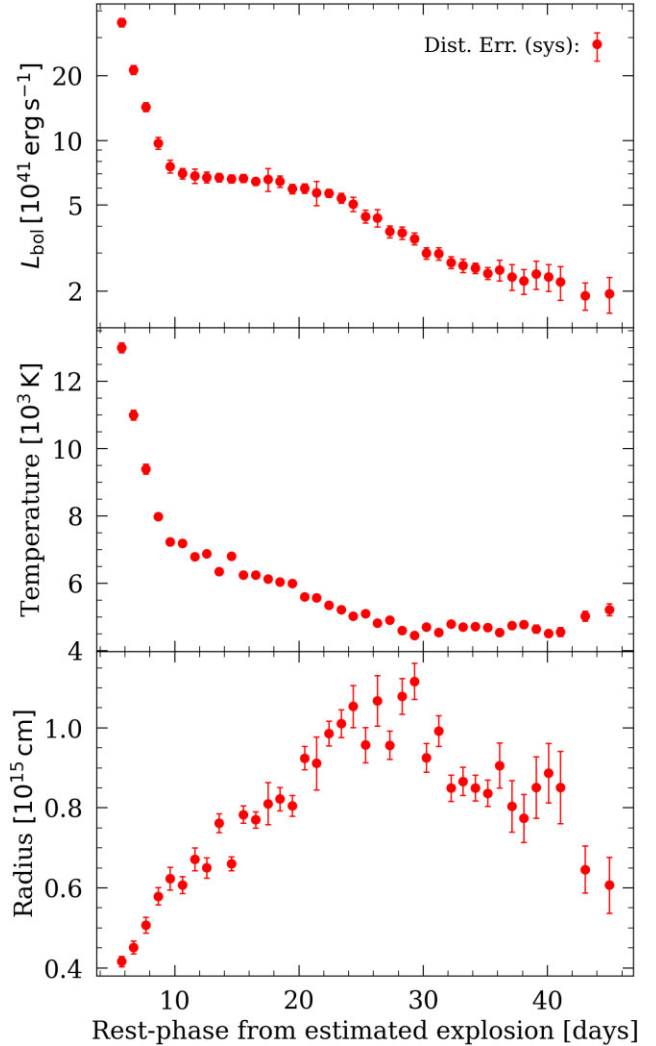
Figure 6. *Top*: Bolometric light curve of SN 2021bxu from integrating the flux in available band with blackbody extrapolation. The systematic error due to the uncertainty in distance is shown as $L_{-16\ \mathrm{per\ cent}}^{+13\ \mathrm{per\ cent}}$. *Middle*: Best-fitting temperature from the blackbody fits. *Bottom*: Radius calculated using the best-fitting blackbody temperature and bolometric luminosity.

are usually found in SN 1987A-like objects (Williams 1987; Tsujimoto & Shigeyama 2001). Sc and Ba have also been observed in the subluminous SN Ia PTF 09dav (Sullivan et al. 2011). This demonstrates that, although SN 2021bxu is formally classified as a SN IIb, it has some spectroscopic similarities to SNe II and SNe Ia.

5.2 Line velocities

We measure the Doppler shift of the minima of the spectral features to determine the velocities and chemical composition of the ejecta. The velocities for He I $\lambda\lambda$5876, 6678, 7065, Hα λ6563, Fe II λ5169, and O I λ7774 are computed using misfits[9] (Holmbo 2020), which is an interactive tool used to measure spectral features in spectra of transients and calculate their errors. Within misfits, we smooth the spectrum by applying a low-pass filter to the Fourier-transformed data as described in Marion et al. (2009) and obtain best-fitting

---

[9] https://github.com/sholmbo/misfits
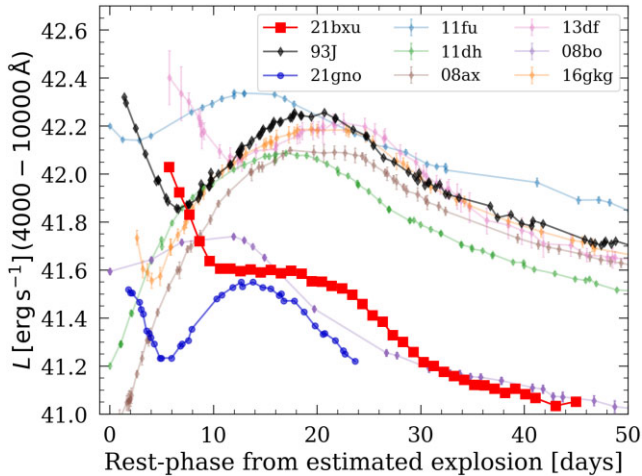
Figure 7. Pseudo-bolometric light curve of SN 2021bxu shown in red compared with a sample of Type IIb SNe from Prentice et al. (2020) and Ca-rich SN 2021gno from Ertini et al. (in preparation) in the range 4000–10 000 Å. The time axis for all SNe has the zero-point at the estimated time of explosion.
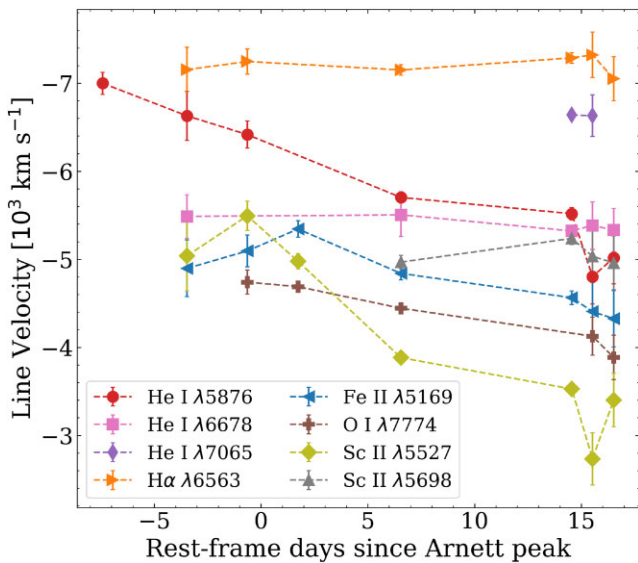
Figure 8. Evolution of line velocities of He $\text{I}\,\lambda5876, \lambda6678, \lambda7065$, H α $\lambda6563$, Fe $\text{II}\,\lambda5169$, O $\text{I}\,\lambda7774$, Sc $\text{II}\,\lambda5527$, and Sc $\text{II}\,\lambda5698$ measured from the spectra using `misfits`. Only those epochs are included for each line where a clear measurement was possible. Note that the Fe $\text{II}\,\lambda5169$ velocity evolution may be uncertain because it comes from a blend of spectral features in the forest of Fe lines.

Gaussians to the absorption features with a fixed local continuum. The best-fitting mean of the Gaussian with the associated error from Monte Carlo iterations is taken to be the absorption feature's observed wavelength which is then converted to a line velocity.

Fig. 8 shows the velocity evolution of the selected features. The velocity of the H α $\lambda6563$ feature stays constant at $\sim 7200\,\text{km s}^{-1}$ from ~10 to ~30 d after explosion, demonstrating that at these early phases the photosphere has already reached the bottom of the H layer. Interestingly, the feature from Si $\text{II}\,\lambda6355$ as seen in Fig. 3 could have some contribution from a high-velocity H α $\lambda6563$ component at $\sim 13,000\,\text{km s}^{-1}$. This also matches with the small feature just bluer to H β $\lambda4861$. Therefore, there could be a detached high-velocity H

component in the ejecta. It may be the case that this comes from interaction with an extended envelope.

The velocity of the He $\text{I}\,\lambda5876$ line decreases as a function of time as the photosphere recedes, from $\sim 7000\,\text{km s}^{-1}$ at Day $+7$ to $\sim 5700\,\text{km s}^{-1}$ at Day $+21$. At these phases the He $\text{I}\,\lambda5876$ line velocity follows the photospheric velocity, after which it plateaus, demonstrating that the base of the He layer is at $\sim 5500\,\text{km s}^{-1}$. This He $\text{I}\,\lambda5876$ line is used to break the Arnett degeneracy in modelling the bolometric light curve (see Section 6). The velocity of the He $\text{I}\,\lambda7065$ line is only measured in the later two spectra, thus not showing its early evolution and making it unreliable for analysis. In SE-SNe the He lines require non-thermal excitation. Therefore, they get stronger over time as the density of the ejecta decreases and the mean free path of the γ-rays can increase (Lucy 1991).

The O $\text{I}\,\lambda7774$ line shows the lowest velocity at $< 4700\,\text{km s}^{-1}$ throughout the time range. This is expected as the progenitor star would have a layered structure prior to explosion where heavier elements are further in, towards the centre of the star. The Fe $\text{II}\,\lambda5169$ feature shows a similar decline in velocity to that of other lines at later times. However, it has slightly higher velocities than oxygen, possibly caused by the fact that there could be primordial Fe-mixing throughout the progenitor star, leading to Fe in the top layers. Due to the Einstein coefficient values of Fe $\text{II}\,\lambda5169$, only a small abundance is sufficient to produce the opacity needed for a strong line. The Sc $\text{II}\,\lambda5698$ line shows higher velocities than the Sc $\text{II}\,\lambda5527$ and Fe $\text{II}\,\lambda5169$ lines. This is potentially due to a metallicity effect or mixing phenomena in the ejecta. However, further spectral modelling is required to disentangle this.

In Fig. 9, we compare our measurements of line velocities with Liu et al. (2016), which provides a spectroscopic sample of SE-SNe, and with Das et al. (2022), which provides spectroscopic measurements for Ca-rich IIb SNe. We compute a rolling median for each SN type with a bin size of 5 d where the shaded regions represent the 16th and 84th percentiles of the distribution in the bin indicating the dispersion of velocities. The sample of SNe IIb has velocities lower than those of SNe Ib for most of the lines with Ca-rich IIb SNe showing velocities similar to those of SNe IIb. All line velocities for SN 2021bxu are consistently lower than the median of all types by at least $\sim 1500\,\text{km s}^{-1}$, emphasizing its uniqueness and implying that the kinetic energy of SN 2021bxu is lower than that of typical SE-SNe.

5.3 Time of explosion

Using line velocities of He $\text{I}\,\lambda5876$ from the spectra (see Section 5.2) along with radii computed from the black-body fits, we trace back to the time of explosion. Assuming a homologous expansion of ejecta, the relation is given by $t_{\text{exp}} \propto R_{\text{BB}}/v_{\text{ph}}$, which becomes $t_{\text{exp}} \approx R_{\text{BB}}/v_{\text{ph}}$ for small initial radius compared to the post-explosion radius of the ejecta. We expect the estimated explosion time to fall between the last non-detection (6.01 d before discovery) and the discovery. We choose measurements from two spectra where the He $\text{I}\,\lambda5876$ velocity is still linearly declining and has not plateaued, ensuring that these values are representative of the photosphere and not the base of the He layer. Using the values $v_{\text{ph}} = \{6600 \pm 300, 6400 \pm 200\}\,\text{km s}^{-1}$ and $R_{\text{BB}} = \{(6.1 \pm 0.2) \times 10^{14}, (7.6 \pm 0.3) \times 10^{14}\}\,\text{cm}$, we obtain the averaged time of explosion within the expected window, at 5.0 ± 0.4 d before discovery, on MJD 59246.3 ± 0.4 d. This is the estimated time of explosion we adopt throughout this paper. The uncertainty on the time of explosion is purely statistical and is appropriately propagated from the uncertainties on radius and velocity.
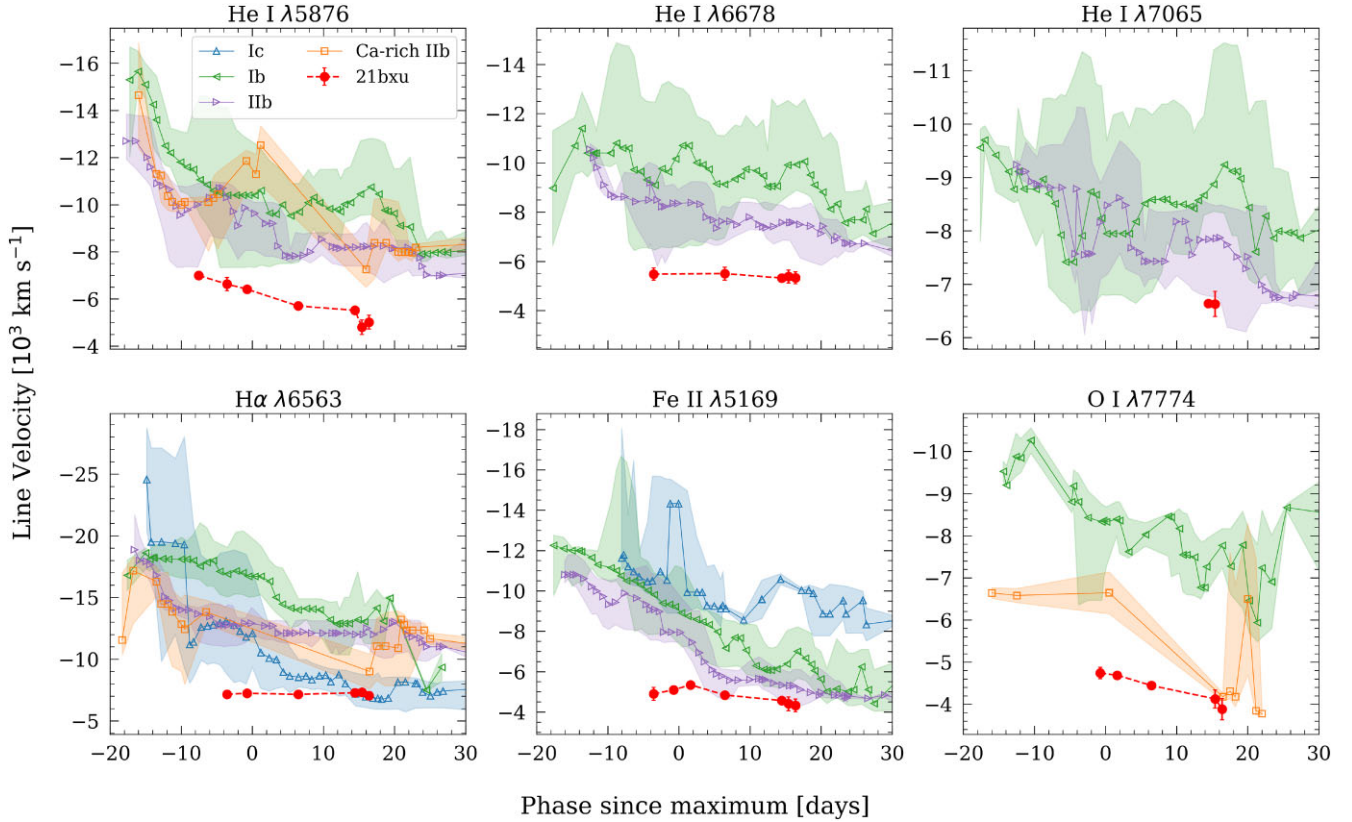
Figure 9. Evolution of line velocities of SN 2021bxu compared to a sample of SNe IIb, Ib, Ic from Liu et al. (2016) and Ca-rich IIb SNe from Das et al. (2022). The open markers show a rolling median for each SN type with a bin size of 5 d where the shaded regions represent the 16th and 84th percentiles of the distribution in the bin indicating the dispersion of velocities. In the case of double-peaked light curves, the phases are relative to the second bolometric peak. Values for SN 2021bxu are shown as filled red circles.

5.4 Spectral comparison with similar supernovae

In this section, we compare the spectrum of SN 2021bxu near the peak due to ^{56}Ni with similar SNe near their peaks. Fig. 10, along with the line IDs, shows spectra for a Type II-pec SN 1987A, a Type IIb SN 1993J, a Ca-rich Type Ib SN 2016hgs and SN 2021gno, and Ca-rich Type IIb SNe 2018gjx, and 2019pof. These SNe, except SN 1987A, are chosen for comparison because of their similarities either in light curve shape or spectral features. SN 1987A is included for its strong H lines showing recombination.

SN 2021bxu is dissimilar to SN 1987A due to the lack of strong hydrogen Balmer features (Hα λ6563, Hβ λ4861, and Hγ λ4340) and also due to the absence of the Na I D $\lambda\lambda$5890, 5896 doublet lines. However, SN 2021bxu does show features from the neutron capture elements Sc II $\lambda\lambda$5527, 5698, 6280, and Ba II λ6142 which are typically seen in SN 1987A-like objects. There are also no signatures of strong H emission, which is usually seen in SNe IIP, hence providing further evidence that the plateau in SN 2021bxu is unlikely to be caused by H-recombination. SN 2021bxu is more similar to SN 1993J, reinforcing the typing of SN 2021bxu as a Type IIb.

Comparing the spectral time series of SN 2021bxu with SN 1993J at similar epochs in Fig. 11, we note that both SNe display similar absorption lines in their spectra. SN 1993J shows broader features at higher velocities between 10 000 and 16 000 km s^{-1} (Garnavich & Ann 1994) compared to the velocities of SN 2021bxu that we measure in the range $4000 < v < 7000$ km s^{-1}. This points to SN 2021bxu having lower energies and masses than SN 1993J. Although they both show similar features, SN 2021bxu evolves more quickly showing

strong metal features from Ca II [IR-triplet] and O I λ7774 by Day 30. The He I λ5876 and He I λ6678 features also quickly get deeper, showcasing the fast evolution of SN 2021bxu. Moreover, SN 1993J shows weaker He I λ5876 absorption than SN 2021bxu but Hα λ6563 absorption of similar depth. Due to their spectral similarities, it may be the case that SN 2021bxu and SN 1993J are similar objects, both with a large initial decline but with different amount of ^{56}Ni, energy and mass. We discuss this further in Section 7.

The Ca-rich SNe show characteristically strong Ca II compared to O I. During the photometric phases, SN 2021bxu shows comparably strong Ca II absorption to that of the Ca-rich Ib and IIb SNe. One of the defining properties of Ca-rich transients is that they quickly transition to nebular phase marked by Ca II and O I emission. For instance, SN 2019ehk (Ca-rich IIb) started exhibiting nebular features as early as 30 d after explosion. SN 2021bxu does not show any nebular features within ~30 d after explosion. Due to the lack of late phase spectra for SN 2021bxu, we cannot directly compare it to Ca-rich SNe using the [Ca II]/[O I] ratio. However, the hydrogen-rich SN 2021bxu shows dissimilarities to the Ca-rich Ib SNe (SN 2021gno, SN 2016hgs), which lack hydrogen in their spectra, but is spectroscopically similar to IIb (SN 1993J) and hydrogen- and Ca-rich IIb SNe (SN 2018gjx) near peak.

6 MODELLING

To understand the origin of the unique shape of SN 2021bxu's light curve, we analyse the explosion by fitting the bolometric and
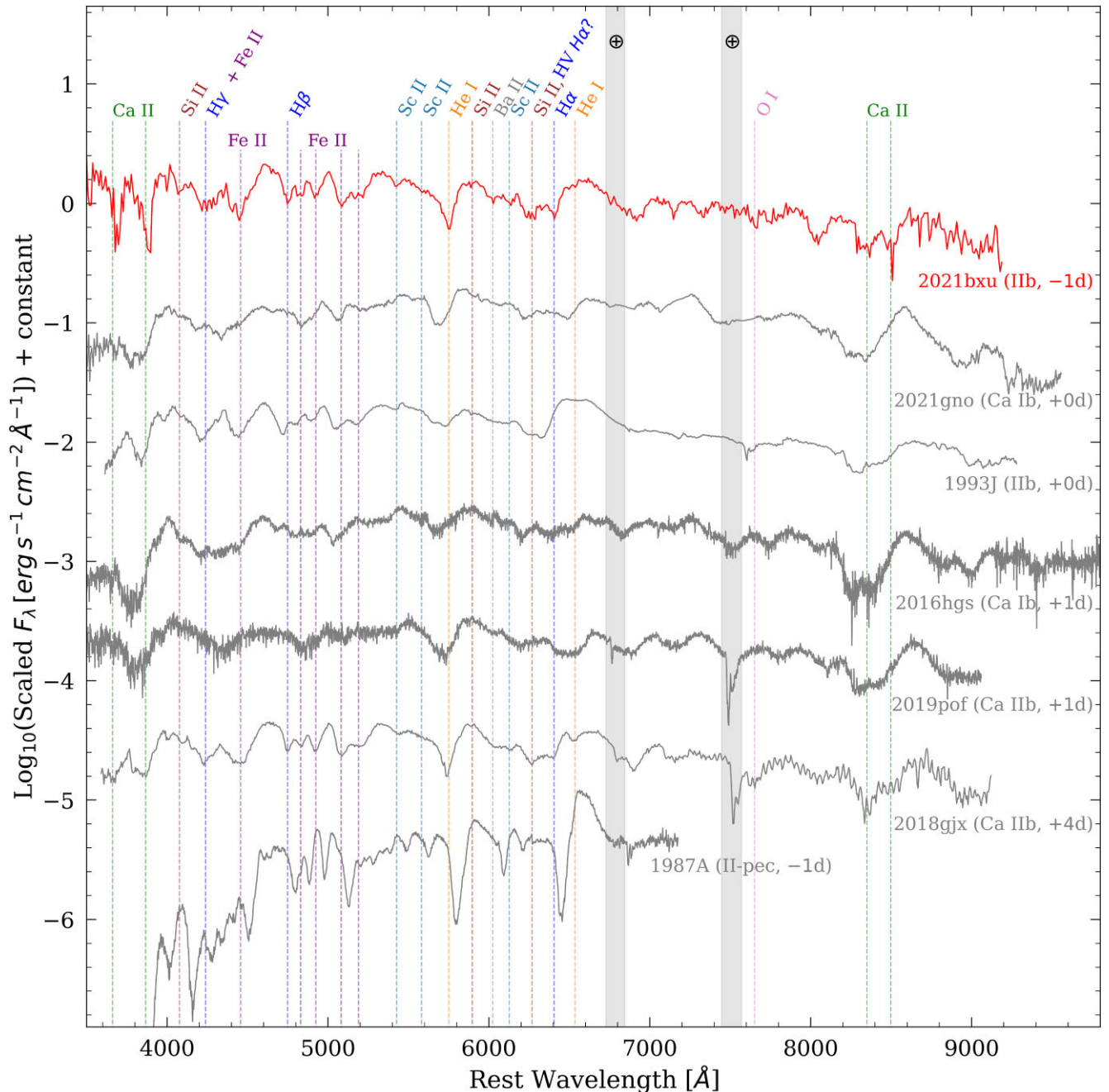
Figure 10. NOT spectrum of SN 2021bxu near the ^{56}Ni peak shown in red compared to the NOT spectrum of Ca-rich Ib SN 2021gno (Ertini et al. in preparation), the Asiago Observatory spectrum of Type IIb SN 1993J (Barbon et al. 1995), the Keck-LRIS spectrum of Ca-rich Type Ib SN 2016hgs (De et al. 2018), the Palomar-200inch spectrum of Ca-rich Type IIb SN 2019pof (Das et al. 2022), the NTT spectrum of Ca-rich Type IIb SN 2018gjx (Prentice et al. 2020), and the International Ultraviolet Explorer (IUE) spectrum of Type II SN 1987A (Pun et al. 1995). Major absorption features in SN 2021bxu are marked on the plot along with the two telluric regions shown in grey bands. All phases in this figure are relative to the ^{56}Ni peak of each SN.

pseudo-bolometric light curves of SN 2021bxu with SN explosion models from the literature. We do this using a two-component model where the first component is the initial cooling phase, and the second component is the radioactive decay of ^{56}Ni including γ-ray leakage.

The analytic model we consider for the initial cooling phase is from Piro et al. (2021, hereafter P21). P21 describes the shock interaction with the extended material surrounding the progenitor star once it is in thermal equilibrium and in homologous expansion phase, given a two-component density profile with steep radial dependence in the outer region and shallower radial dependence in the inner region. The

free parameters in this model are the mass and radius of the extended material (M_e and R_e, respectively) with E_e, the energy imparted by the SN shock to the extended material, depending on the total explosion energy, ejecta mass, and mass of the extended material. The analytic model from P21 is an improvement over previous similar models (e.g. Piro & Nakar 2013; Piro 2015) as it better matches the observations in the early shock-cooling emission and is tested against numerical models.

Together with the P21 model, we use the analytic models from Arnett (1982, hereafter A82) for the plateau/secondary peak from
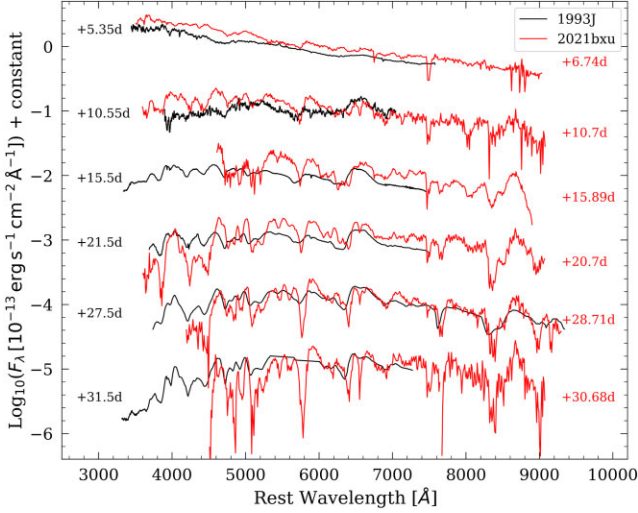
Figure 11. Spectral comparison of SN 2021bxu with SN 1993J. The spectra for SN 1993J are shown in black with the epochs labelled on the left. The spectra for SN 2021bxu are shown in red with the epochs labelled on the right. For both objects, the epochs are relative to the estimated time of explosion. The spectra at +5.35, +10.55, +21.5, and +27.5 d for SN 1993J are from Barbon et al. (1995), +15.5 d is from Matheson et al. (2000b), and +31.5 d is from Matheson et al. (2000a).

^{56}Ni decay, which provides an estimate of the total ejecta mass ($M_{\rm ej}$), ^{56}Ni mass ($M_{\rm Ni}$), and total explosion energy of the SN ($K_{\rm ej}$). We adopt a mean optical opacity of $\bar{\kappa}_{\rm opt} = 0.1\,{\rm cm}^2\,{\rm g}^{-1}$ corresponding to electron scattering. The A82 model fits for a degenerate parameter that depends on $M_{\rm ej}$ and $K_{\rm ej}$ as $M_{\rm ej}^{3/4}/K_{\rm ej}^{1/4}$. This degeneracy is broken using the velocity of the He Iλ5876 line near maximum of the ^{56}Ni peak to obtain the ejecta expansion velocity (see section 5.3 of Dessart et al. 2016). After interpolating between the spectral epochs, we use $v_{\rm ej} = 4900 \pm 200\,{\rm km\,s}^{-1}$ near peak. We include an additional correction for γ-ray leakage at late times as shown by Wheeler, Johnson & Clocchiatti (2015, hereafter W15) with a multiplicative factor of $1 - {\rm e}^{-(T_0/t)^2}$, where T_0 is the characteristic time-scale for the γ-ray leakage, depending on $M_{\rm ej}$ and $K_{\rm ej}$ as

$$T_0 = \left(\frac{C \kappa_\gamma M_{\rm ej}^2}{K_{\rm ej}} \right)^{1/2}, \tag{1}$$

where C is a dimensionless structure constant dependent on the slope of the density profile (typically $C \sim 0.05$) and κ_γ is the opacity to γ-rays (fiducial value of $\kappa_\gamma = 0.03\,{\rm cm}^2\,{\rm g}^{-1}$).

We adopt a chi-squared minimization approach to fit the bolometric and pseudo-bolometric light curves of SN 2021bxu and obtain the best-fitting parameters. Nakar & Piro (2014) give a relation between the P21 parameters E_e and M_e along with a dependency on the A82 parameters $M_{\rm ej}$ and $K_{\rm ej}$,

$$E_e \approx 2 \times 10^{49} \left(\frac{K_{\rm ej}}{10^{51}\,{\rm erg}} \right) \left(\frac{M_{\rm ej}}{3\,{\rm M}_\odot} \right)^{-0.7} \left(\frac{M_e}{0.01\,{\rm M}_\odot} \right)^{0.7} {\rm erg.} \tag{2}$$

Therefore, we eliminate E_e from the fitting routine and later solve for it using equation (2). With only approximately five data points in the initial decline, the parameters from P21 for the early light curve are difficult to constrain. However, the model fits well the later part where A82 + W15 dominates and there are more points to fit. Changing the initial decline of the light curve barely affects the second component assumed from ^{56}Ni decay. The best-fitting parameters are given by the maximum-likelihood values and the uncertainties on best-fitting
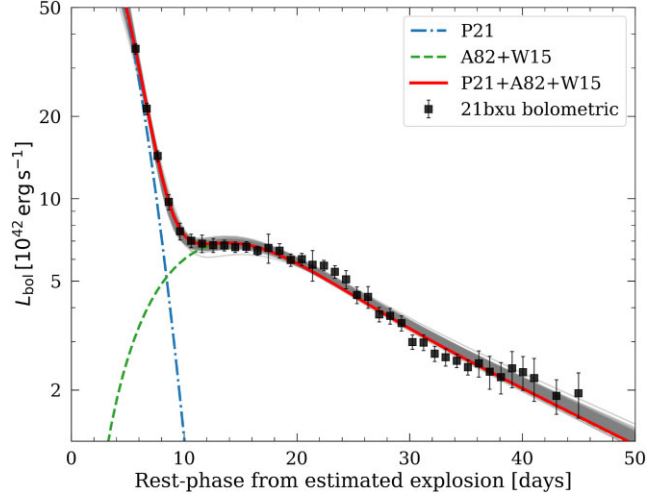

Figure 12. Bolometric light curve of SN 2021bxu shown in black fit using a two-component model: shock cooling and ^{56}Ni decay including γ-ray leakage. The initial decline is fit with the shock interaction with extended envelope model from Piro et al. (2021) shown as the dot–dashed line and ^{56}Ni decay comes from the model from Arnett (1982) following an additional correction for γ-ray leakage as shown by Wheeler et al. (2015) shown as the dashed line. The best-fitting model is the solid red line and the grey lines show 100 randomly selected parameters from the Monte Carlo samples signifying the uncertainty on the best fit.

Table 4. Best-fitting parameters after fitting the P21 + A82 + W15 model to the bolometric and pseudo-bolometric light curves.

Parameter	Bolometric	Pseudo-bolometric (4000–10 000 Å)
$M_{\rm Ni}$ [M$_\odot$]	$0.029^{+0.004}_{-0.005}$	$0.017^{+0.002}_{-0.003}$
$M_{\rm ej}$ [M$_\odot$]	$0.61^{+0.06}_{-0.05}$	$0.55^{+0.06}_{-0.05}$
$K_{\rm ej}$ [10^{49} erg]	$8.8^{+1.1}_{-1.0}$	$7.9^{+1.1}_{-1.0}$
E_e [10^{49} erg]	$2.0^{+0.4}_{-0.3}$	$2.1^{+0.6}_{-0.3}$
M_e [M$_\odot$]	$0.065^{+0.005}_{-0.005}$	$0.076^{+0.011}_{-0.010}$
R_e [R$_\odot$]	1400^{+300}_{-200}	370^{+100}_{-50}

parameters are given by the 16th and 84th percentiles from fitting the model to Monte Carlo resamples of the light curve. The uncertainties for the parameters derived using the best-fitting values are propagated appropriately from the uncertainties on the best-fitting values. The Monte Carlo resampling ensures that statistical uncertainties from the photometry as well as systematic uncertainties from distance measurement are appropriately considered.

When fitting the bolometric and pseudo-bolometric light curves, we find that the P21 + A82 + W15 model can successfully describe the data. Fig. 12 shows the two components separately as well as the combined fit in red for the bolometric light curve. The surrounding grey region is randomly drawn Monte Carlo samples showing the uncertainty on the best-fitting model. The best-fitting parameters for the bolometric and pseudo-bolometric light curve fits are listed in Table 4. The parameters for the pseudo-bolometric light curve are provided because they are useful in direct comparison with pseudo-bolometric light curves from literature. It should be noted that the pseudo-bolometric light curves do not encompass the total flux and hence one must be cautious when inferring physical parameters from them.
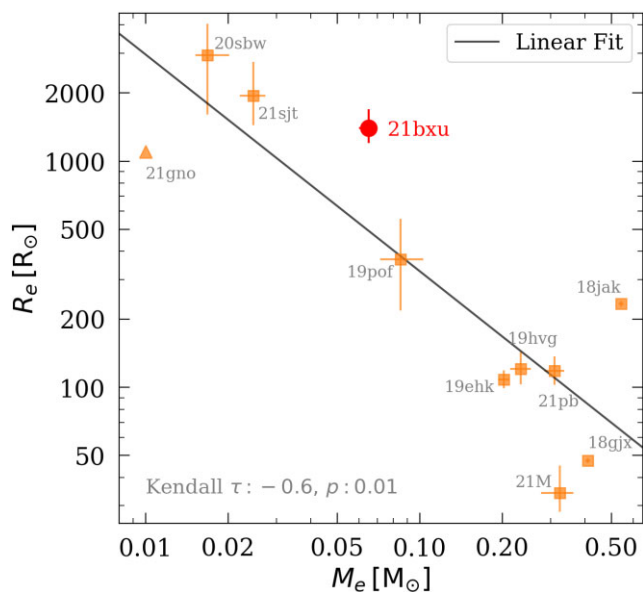
Figure 13. Mass and radius of the extended material (M_e and R_e, respectively) from fitting the initial decline of SN 2021bxu compared with the sample of Ca-rich SNe IIb (Das et al. 2022) and the Ca-rich Ib SN 2021gno (Ertini et al. in preparation). The values for Ca-rich SNe IIb (orange squares) and SN 2021bxu (red circle) are obtained from fitting the P21 model and the values for SN 2021gno (orange triangle) are obtained using a hydrodynamic code from Bersten, Benvenuto & Hamuy (2011). We note a trend of decreasing radius with increasing mass with a linear best-fitting shown as the black line and Kendall τ correlation statistic given.

7 DISCUSSION

In this section, we attempt to put our results in context relative to other SN explosions and models. The best-fitting parameters for the bolometric light curve are $M_{\rm Ni} = 0.029^{+0.004}_{-0.005}\,{\rm M_\odot}$, $M_{\rm ej} = 0.61^{+0.06}_{-0.05}\,{\rm M_\odot}$, $K_{\rm ej} = 8.8^{+1.1}_{-1.0} \times 10^{49}$ erg, $E_e = 2.0^{+0.4}_{-0.3} \times 10^{49}$ erg, $M_e = 0.065^{+0.005}_{-0.005}\,{\rm M_\odot}$, and $R_e = 1400^{+300}_{-200}\,{\rm R_\odot}$ (listed in Table 4). SN 2021bxu is a Type IIb SN with low $M_{\rm Ni}$, low luminosity, and low explosion energy. By comparison with known classes of SNe and models explaining the observed features of SN 2021bxu, we can infer the details of the explosion and the progenitor system.

The fit to the P21 model shows that the extended material surrounding the progenitor of SN 2021bxu had a large radius (R_e) and low mass (M_e). We compare this to the best-fitting masses and radii of the Ca-rich IIb sample from Das et al. (2022), who use the same model for the initial decline. Fig. 13 shows SN 2021bxu along with the sample of Ca-rich IIb SNe. We see a clear trend of decreasing radius with increasing mass. The Ca-rich Ib SN 2021gno also falls along this trend with $R_e = 1100\,{\rm R_\odot}$ and $M_e = 0.01\,{\rm M_\odot}$. For a simple check, we show a linear best fit and a negative correlation using the Kendall τ test. The best-fitting line is given by $\log_{10}(R_e) = -0.96\log_{10}(M_e) + 1.55$ with a root-mean-square deviation of 0.16 dex. The Kendall τ test gives $\tau = -0.6$ with a p-value of 0.01. Modelling and possible physical origins of this correlation will be the subject of a future work.

Theory suggests that a plateau can arise in the light curve of a SE-SN $\sim$1 d after shock-breakout when the cooling of the photosphere slows down, allowing the recombination of ejecta layers, primarily He (Dessart et al. 2011). Observed in simulations by Dessart et al. (2011), this plateau is found at $\log(L_{\rm bol}/{\rm erg\,s^{-1}}) \sim 41$ and lasts for $\sim$10 d until the SN either re-brightens for ^{56}Ni-rich SNe or fades away for ^{56}Ni-poor SNe. The plateau in SN 2021bxu is
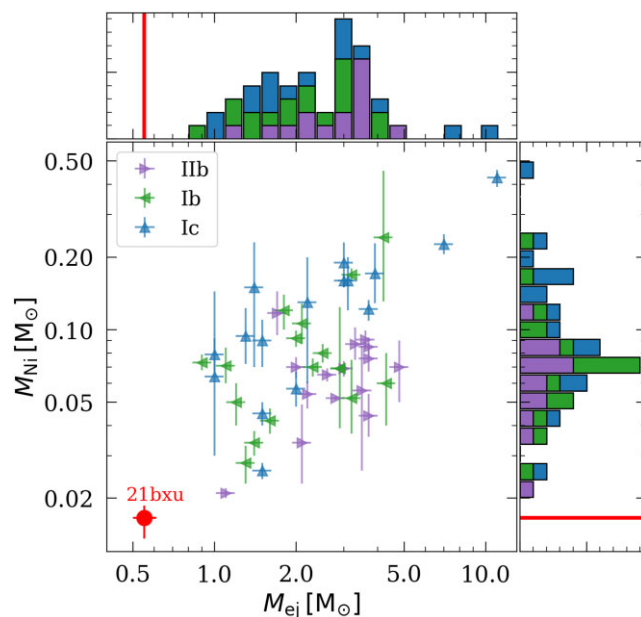

Figure 14. Distributions of $M_{\rm Ni}$ and $M_{\rm ej}$ derived using the pseudo-bolometric light curves in the range 4000–10 000 Å for the sample of SNe IIb, Ib, Ic from Prentice et al. (2016, 2019). The values for SN 2021bxu are shown in red.

observed for a time-scale comparable to that of He-recombination; however, the timing of occurrence differs. The plateau caused by He-recombination occurs soon after explosion, whereas the plateau in SN 2021bxu's light curve is not apparent until $\sim$10 d after explosion. Moreover, the luminosity of SN 2021bxu at the plateau is $\log(L_{\rm bol}/{\rm erg\,s^{-1}}) \sim 41.8$, almost an order of magnitude higher. This suggests that the observed plateau in SN 2021bxu is likely not due to He-recombination.

SN 2021bxu shows photometric and spectroscopic similarities to SN 1993J but with lower total mass and explosion energy. SN 1993J shows an initial decline due to the post-shock cooling through a thin H-rich envelope of extended material and the main peak from ^{56}Ni decay. Bersten et al. (2012) and Prentice et al. (2016) estimate $M_{\rm Ni}$ in the range 0.084–0.15 M$_\odot$ and $M_{\rm ej} = 3.3\,{\rm M_\odot}$ from fitting the bolometric light curve of SN 1993J. This is approximately three to five times more ^{56}Ni mass than in SN 2021bxu and approximately six times more ejecta mass. Higher $M_{\rm Ni}$ and $M_{\rm ej}$ lead to the main ^{56}Ni powered light curve to be more luminous and broader, respectively, which is seen in the light curve of SN 1993J. The light curve of SN 1993J has been described by a binary model with both stars having a mass of $\sim 15\,{\rm M_\odot}$ (Nomoto et al. 1993; Podsiadlowski et al. 1993). The authors conclude that SN 1993J had a G8-K0 yellow supergiant progenitor with a binary companion. The strong initial decline can be explained by the explosion of this progenitor that has experienced mass-loss due to winds, or, more likely, through mass transfer to a companion star. Given that SN 2021bxu is a similar object to SN 1993J at least in the initial decline and a two-component light curve, SN 2021bxu may be conspiring to show a plateau instead of an evident second peak owing to the small amount of ^{56}Ni produced and the overall lower energies.

For a direct comparison with other studies without dealing with the SED flux extrapolation problems, we use the ^{56}Ni mass and the ejecta mass derived from pseudo-bolometric light curves. Fig. 14 shows the best-fitting parameters for SN 2021bxu from the pseudo-bolometric light curve compared to a sample of SNe IIb, Ib, Ic from Prentice et al. (2016, 2019). In order to obtain the pseudo-bolometric light

curve in the range 4000–10 000 Å, Prentice et al. (2016, 2019) use *BVRI*-bands and fit the A82 model to find the best-fitting parameters, mainly M_{Ni} and M_{ej}. SN 2021bxu shows the lowest value of the entire SE-SNe sample for M_{Ni} and M_{ej} as derived from the pseudo-bolometric light curves.

Fully bolometric light curves are a better probe of the physical parameters than pseudo-bolometric light curves. Fig. 15 shows the best-fitting parameters from the bolometric light curve compared to a sample of SNe IIb, Ib, Ic from Prentice et al. (2016) and Ca-rich IIb SNe from Das et al. (2022). As seen in Fig. 15, M_{Ni} for SN 2021bxu is also the lowest in the bolometric sample of SE-SNe; the only lower values being that of the ultra-stripped SNe (US-SNe). K_{ej} for SN 2021bxu is also on the lower end of the comparison sample. M_{ej} for SN 2021bxu is closer to more common values and falls in the category of strongly stripped SNe (SS-SNe). However, the best-fitting parameters from a full bolometric light curve should be interpreted cautiously because the contribution to the total luminosity from the unobserved wavelengths is highly uncertain and treated differently by different studies. For example, Prentice et al. (2016) assume a 10 per cent contribution from the unobserved wavelengths after considering *UBVRI*-bands and near-IR. In this study, we assume a blackbody SED for extrapolation to the unobserved wavelengths after direct integration in the observed bands.

Observed properties like low ejecta mass, low peak luminosity, faster-than-normal photometric and spectroscopic evolution are exhibited by the Ca-rich class of transients. They reach nebular phase quickly within as low as ∼1 month after explosion (e.g. Shen et al. 2019; Nakaoka et al. 2021; Das et al. 2022). CC Ca-rich transients are characterized by the presence of strong helium spectral features near peak and the appearance of calcium emission soon after. However, we do not find any strong calcium emission lines in the spectra, at least at the early epochs of ∼31 d after explosion. In SN 2021bxu, the presence of hydrogen along with neutron capture elements rules out most systems with WD progenitors.

The current popular theory suggests that Ca-rich SNe could result from low-mass He stars ($M_{ZAMS} \sim 8$–$12 \, M_\odot$) that are highly stripped down to less than $\sim 3 \, M_\odot$, suggesting a new class of SS-SNe (e.g. Das et al. 2022; Ertini et al. in preparation). SS-SNe form a transition class between SE-SNe and ultra-stripped SNe (US-SNe; Tauris et al. 2015; Das et al. 2022). As a result of their low initial masses, the resultant ejecta masses are also low (less than $\sim 1 \, M_\odot$) along with low ^{56}Ni masses. Ertini et al. (in preparation) showed that the progenitor scenario of the Ca-rich SN 2021gno can be modelled with a highly stripped massive star with an ejecta mass of $0.8 \, M_\odot$ and a ^{56}Ni mass of $0.024 \, M_\odot$, comparable to the values for SN 2021bxu. We see in Fig. 15 that SN 2021bxu has M_{ej} consistent with the sample of Ca-rich IIb SNe and in the range demarcating SS-SNe, but M_{Ni} and K_{ej} are on the lowest end of the distribution.

Ca-rich IIb SNe are usually found in star-forming regions of galaxies and at smaller separations from the centre of the host galaxy compared to Type I Ca-rich transients (Das et al. 2022). As seen in Section 2, the host galaxy ESO 478- G 006 is a star-forming galaxy with an SFR of $33^{+16}_{-27} \, M_\odot \, yr^{-1}$, typical of the hosts of Ca-rich IIb SNe (Das et al. 2022). The projected physical offset of SN 2021bxu from its host is $9.2 \pm 0.6 \, kpc$, which is again typical for Ca-rich IIb SNe and SE-SNe (Das et al. 2022). Despite its similarities with Ca-rich IIb SNe, the lack of nebular spectra of SN 2021bxu showing Ca II emission makes it difficult to conclusively judge whether SN 2021bxu is a Type IIb Ca-rich SN. Nevertheless, SN 2021bxu is an interesting object and shows that stars can explode with a small M_{ej} and K_{ej} with a large radius while making small amounts of ^{56}Ni.

8 CONCLUSION

In this study, we present observations and analysis of a unique SE-SN, SN 2021bxu. As discussed in Section 4, we show that SN 2021bxu had a large initial decline in brightness followed by a short plateau not caused by H- or He-recombination, which is unusual for a Type IIb SN. It is on the faint end of the sample of SE-SNe from the literature, with the peak absolute magnitude of $M_r = -16.86 \pm 0.16 \, mag$ and the average absolute magnitude during the plateau of $M_r \sim -15.9 \, mag$. The pseudo-bolometric luminosity is also fainter compared to most other SE-SNe, with a peak of $\log(L_{pseudo}/erg \, s^{-1}) = 42.0$ and a distinct plateau phase at $\log(L_{pseudo}/erg \, s^{-1}) \sim 41.6$. The overall light curve shape in *gri*-bands matches most closely to that of Ca-rich IIb SNe, most of which show an initial decline and a second peak, and to that of SNe IIb. The initial decline in the light curve of SN 2021bxu has a similar slope to the initial decline of SN 1993J but SN 1993J shows a distinct second peak from ^{56}Ni at $\log(L_{pseudo}/erg \, s^{-1}) = 42.23$ and has a slower evolution at late-times indicating a larger ejecta mass.

With the presence of strong helium lines and weaker hydrogen lines, SN 2021bxu is a Type IIb SN (Section 5). We constrain the time of explosion using the He I λ5876 line velocity and the blackbody radius evolution and find it to be $5.0 \pm 0.4 \, d$ before discovery. It evolves quickly to show absorption features from heavier metals like oxygen, calcium, silicon, iron, and neutron capture elements like barium and scandium, which get stronger over the 30-d spectral time series. We note that SN 2021bxu shows spectral similarities to Type IIb SN 1993J as well as to Ca-rich IIb SNe during photometric phases with most of the same features observed. SN 1993J has velocities higher by a factor of ∼2 compared to SN 2021bxu. We also note similarities to SN 2021gno in terms of light curve evolution and modelling. From a photometric and spectroscopic analysis, we conclude that SN 2021bxu is a fast-evolving SN, with a short distinct plateau phase not caused by H- or He-recombination and with some of the lowest observed line velocities compared to samples of Ca-rich IIb SNe and SE-SNe.

Following the modelling of the bolometric and pseudo-bolometric light curves in Section 6, we see that the light curves of SN 2021bxu can be well modelled by a composite model including interaction of the shock with an extended envelope of material surrounding the progenitor and the normal radioactive decay of ^{56}Ni. We obtain the physical parameters for the explosion such as M_{Ni}, M_{ej}, K_{ej}, and T_0, and the properties of the extended material E_e, M_e, and R_e from bolometric and pseudo-bolometric light curves (see Table 4). Ertini et al. (in preparation) performed hydrodynamic modelling of SN 2021gno and similarly showed that the initial cooling phase can be explained by extended circumstellar material composed mainly of He, maybe with traces of H, and the second peak can be explained by the radioactive decay of ^{56}Ni. We note that the ^{56}Ni mass and kinetic energy for SN 2021bxu are on the lower end of the distribution for Ca-rich SNe and SE-SNe. The ejecta mass falls within the range of Ca-rich SNe and SS-SNe.

Overall we determine that SN 2021bxu likely occurred from a lower mass progenitor which had a large radius at the time of explosion and an extended envelope having experienced mass-loss potentially to a companion star, similar either to the SN 1993J scenario or to the strongly stripped Ca-rich SNe such as SN 2021gno. However, to fully understand and characterize explosions similar to SN 2021bxu and to better constrain the parameters of the initial decline in an effort to constrain the immediate surroundings of the progenitor, further high precision multiband observations of SNe in their infant stages are needed. POISE promises to deliver such a data
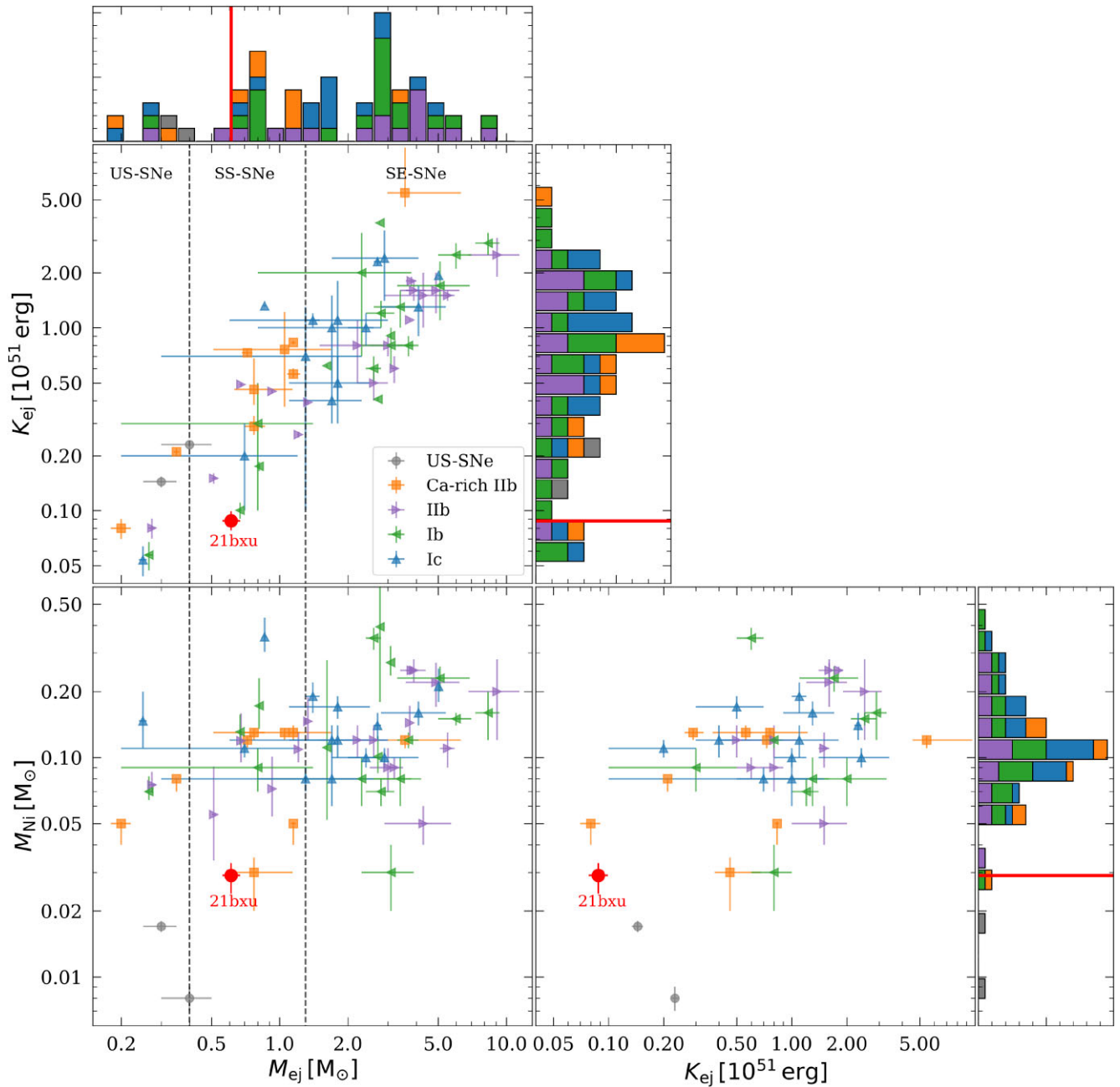
Figure 15. Comparison of SN 2021bxu with a sample of SNe IIb, Ib, Ic from Taddia et al. (2018) and Prentice et al. (2016), Ca-rich IIb SNe from Das et al. (2022), and US-SNe from De et al. (2018) and Yao et al. (2020). The ^{56}Ni mass (M_{Ni}), ejecta mass (M_{ej}), and kinetic energy (K_{ej}) are derived using the full bolometric light curves for all SNe. The vertical dashed lines indicate the rough boundaries dividing ultra-stripped SNe (US-SNe), strongly stripped SNe (SS-SNe), and stripped-envelope SNe (SE-SNe; Das et al. 2022). The values for SN 2021bxu are shown in red in each panel.

set over the coming years. In addition to the early-time data, late-time data for such objects in the nebular phase would also prove beneficial in discerning if they are Ca-rich transients and allude to new classes such as SS-SNe.

DATA AVAILABILITY

The photometry presented in this paper is available in a machine-readable format from the online journal as supplementary material. A portion is shown in Tables A1, A2, and A3 for guidance regarding its form and content. The spectra presented in this paper are available via the WISeREP[10] archive (Yaron & Gal-Yam 2012).

REFERENCES

Anderson J. P. et al., 2014, ApJ, 786, 67
Arcavi I. et al., 2011, ApJ, 742, L18
Arnett W. D., 1982, ApJ, 253, 785 (A82)
Ashall C. et al., 2022, ApJ, 932, L2
Barbon R., Benetti S., Cappellaro E., Patat F., Turatto M., Iijima T., 1995, A&AS, 110, 513
Bellm E. C. et al., 2019, PASP, 131, 018002
Benvenuto O. G., Bersten M. C., Nomoto K., 2013, ApJ, 762, 74
Bersten M. C., Benvenuto O., Hamuy M., 2011, ApJ, 729, 61
Bersten M. C. et al., 2012, ApJ, 757, 31

Bose S., Kumar B., Misra K., Matsumoto K., Kumar B., Singh M., Fukushima D., Kawabata M., 2016, MNRAS, 455, 2712
Breeveld A. A., Landsman W., Holland S. T., Roming P., Kuin N. P. M., Page M. J., 2011, in McEnery J. E., Racusin J. L., Gehrels N.eds, AIP Conf. Proc. Vol. 1358, Gamma Ray Bursts 2010. Am. Inst. Phys., New York, p. 373
Brown P. J., Breeveld A. A., Holland S., Kuin P., Pritchard T., 2014, A&SS, 354, 89
Bruzual G., Charlot S., 2003, MNRAS, 344, 1000
Burns C. et al., 2021, Astron. Telegram, 14441, 1
Buzzoni B. et al., 1984, The Messenger, 38, 9
Cardelli J. A., Clayton G. C., Mathis J. S., 1989, ApJ, 345, 245
Carnall A. C., 2017, preprint (arXiv:1705.05165)
Chambers K. C. et al., 2016, preprint (arXiv:1612.05560)
Cid Fernandes R., Mateus A., Sodré L., Stasińska G., Gomes J. M., 2005, MNRAS, 358, 363
Clocchiatti A., Wheeler J. C., Benetti S., Frueh M., 1996, ApJ, 459, 547
Das K. K. et al., 2022, preprint (arXiv:2210.05729)
De K. et al., 2018, ApJ, 866, 72
de Jaeger T. et al., 2020, MNRAS, 495, 4860
de Vaucouleurs G., de Vaucouleurs A., Corwin Herold G. J., Buta R. J., Paturel G., Fouque P., 1991, S&T, 82, 621
DerKacy J., 2021, Transient Name Server Classification Report, 2021-447, 1
DerKacy J. M. et al., 2023, MNRAS, 522, 3481
Dessart L., Hillier D. J., Livne E., Yoon S.-C., Woosley S., Waldman R., Langer N., 2011, MNRAS, 414, 2985
Dessart L., Hillier D. J., Woosley S., Livne E., Waldman R., Yoon S.-C., Langer N., 2016, MNRAS, 458, 1618
Dressler A. et al., 2011, PASP, 123, 288
Faran T. et al., 2014, MNRAS, 445, 554
Fausnaugh M. M. et al., 2021, ApJ, 908, 51
Filippenko A. V., 1997, ARA&A, 35, 309
Filippenko A. V., Matheson T., Barth A. J., 1994, AJ, 108, 2220
Flewelling H. A. et al., 2020, ApJS, 251, 7
Folatelli G. et al., 2013, ApJ, 773, 53
Fraser M. et al., 2021, preprint (arXiv:2108.07278)
Galbany L. et al., 2014, A&A, 572, A38
Galbany L. et al., 2016, MNRAS, 455, 4087
Galbany L. et al., 2018, ApJ, 855, 107
Garnavich P. M., Ann H. B., 1994, AJ, 108, 1002
Gehrels N. et al., 2004, ApJ, 611, 1005
Hamuy M. et al., 2006, PASP, 118, 2
Heger A., Fryer C. L., Woosley S. E., Langer N., Hartmann D. H., 2003, ApJ, 591, 288
Hillebrandt W., Nomoto K., Wolff R. G., 1984, A&A, 133, 175
Holmbo S., 2020, Phd Thesis, Aarhus University
Hook I. M., Jørgensen I., Allington-Smith J. R., Davies R. L., Metcalfe N., Murowinski R. G., Crampton D., 2004, PASP, 116, 425
Janka H.-T., 2012, Annu. Rev. Nucl. Part. Sci., 62, 407
Kasliwal M. M. et al., 2012, ApJ, 755, 161
Kawabata K. S. et al., 2010, Nature, 465, 326
Klingler N. J. et al., 2019, ApJS, 245, 15
Kochanek C. S. et al., 2017, PASP, 129, 104502
Kogure T., Hirata R., 1982, Bull. Astron. Soc. India, 10, 281
Kriek M., van Dokkum P. G., Labbé I., Franx M., Illingworth G. D., Marchesini D., Quadri R. F., 2009, ApJ, 700, 221
Krisciunas K. et al., 2017, AJ, 154, 211
Landolt A. U., 1992, AJ, 104, 340
Liu Y.-Q., Modjaz M., Bianco F. B., Graur O., 2016, ApJ, 827, 90
López-Cobá C. et al., 2020, AJ, 159, 167
Lucy L. B., 1991, ApJ, 383, 308
Magnier E. A. et al., 2020a, ApJS, 251, 3
Magnier E. A. et al., 2020b, ApJS, 251, 6
Marion G. H., Höflich P., Gerardy C. L., Vacca W. D., Wheeler J. C., Robinson E. L., 2009, AJ, 138, 727
Martinez L. et al., 2022, A&A, 660, A40
Masci F. J. et al., 2019, PASP, 131, 018003
Massa D., 1975, PASP, 87, 777

[10]https://www.wiserep.org/

Matheson T. et al., 2000a, AJ, 120, 1487
Matheson T., Filippenko A. V., Ho L. C., Barth A. J., Leonard D. C., 2000b, AJ, 120, 1499
Matheson T., Filippenko A. V., Li W., Leonard D. C., Shields J. C., 2001, AJ, 121, 1648
Miyaji S., Nomoto K., 1987, ApJ, 318, 307
Miyaji S., Nomoto K., Yokoi K., Sugimoto D., 1980, PASJ, 32, 303
Morales-Garoffolo A. et al., 2014, MNRAS, 445, 1647
Morales-Garoffolo A. et al., 2015, MNRAS, 454, 95
Nakaoka T. et al., 2021, ApJ, 912, 30
Nakar E., Piro A. L., 2014, ApJ, 788, 193
Nomoto K., 1984, ApJ, 277, 791
Nomoto K., 1987, ApJ, 322, 206
Nomoto K., Sparks W. M., Fesen R. A., Gull T. R., Miyaji S., Sugimoto D., 1982, Nature, 299, 803
Nomoto K., Suzuki T., Shigeyama T., Kumagai S., Yamaoka H., Saio H., 1993, Nature, 364, 507
Osterbrock D. E., Ferland G. J., 2006, Astrophysics of Gaseous Nebulae and Active Galactic Nuclei. University Science Books, New York
Owocki S., 2006, in Kraus M., Miroshnichenko A. S.eds, ASP Conf. Ser. Vol. 355, Stars with the B[e] Phenomenon. Astron. Soc. Pac., San Francisco, p. 219
Pauldrach A. W. A., Vanbeveren D., Hoffmann T. L., 2012, A&A, 538, A75
Pedregosa F. et al., 2011, J. Mach. Learn. Res., 12, 2825
Perets H. B., Gal-yam A., Crockett R. M., Anderson J. P., James P. A., Sullivan M., Neill J. D., Leonard D. C., 2011, ApJ, 728, L36
Pessi P. J. et al., 2019, MNRAS, 488, 4239
Phillips M. M. et al., 2013, ApJ, 779, 38
Phillips M. M. et al., 2019, PASP, 131, 014001
Piro A. L., 2015, ApJ, 808, L51
Piro A. L., Nakar E., 2013, ApJ, 769, 67
Piro A. L., Haynie A., Yao Y., 2021, ApJ, 909, 209 (P21)
Podsiadlowski P., Hsu J. J. L., Joss P. C., Ross R. R., 1993, Nature, 364, 509
Podsiadlowski P., Langer N., Poelarends A. J. T., Rappaport S., Heger A., Pfahl E., 2004, ApJ, 612, 1044
Poelarends A. J. T., Herwig F., Langer N., Heger A., 2008, ApJ, 675, 614
Prentice S. J., Mazzali P. A., 2017, MNRAS, 469, 2672
Prentice S. J. et al., 2016, MNRAS, 458, 2973
Prentice S. J. et al., 2019, MNRAS, 485, 1559
Prentice S. J. et al., 2020, MNRAS, 499, 1450
Pumo M. L. et al., 2009, ApJ, 705, L138
Pun C. S. J. et al., 1995, ApJS, 99, 223
Richmond M. W., Treffers R. R., Filippenko A. V., Paik Y., Leibundgut B., Schulman E., Cox C. V., 1994, AJ, 107, 1022
Ricker G. R. et al., 2016, in MacEwen H. A., Fazio G. G., Lystrup M., Batalha N., Siegler N., Tong E. C.eds, Proc. SPIE Conf. Ser. Vol. 9904, Space Telescopes and Instrumentation 2016: Optical, Infrared, and Millimeter Wave. SPIE, Bellingham, p. 99042B
Roming P. W. A. et al., 2005, Space Sci. Rev., 120, 95
Salpeter E. E., 1955, ApJ, 121, 161
Schlafly E. F., Finkbeiner D. P., 2011, ApJ, 737, 103
Scolnic D. M. et al., 2018, ApJ, 859, 101
Shappee B. J. et al., 2014, ApJ, 788, 48
Shen K. J., Quataert E., Pakmor R., 2019, ApJ, 887, 180
Shingles L. et al., 2021, Transient Name Server AstroNote, 7, 1
Shivvers I. et al., 2017, PASP, 129, 054201
Smartt S. J. et al., 2015, A&A, 579, A40
Smith N., Owocki S. P., 2006, ApJ, 645, L45
Smith J. A. et al., 2002, AJ, 123, 2121
Smith K. W. et al., 2020, PASP, 132, 085002
Stritzinger M. D. et al., 2018a, A&A, 609, A134
Stritzinger M. D. et al., 2018b, A&A, 609, A135
Sukhbold T., Ertl T., Woosley S. E., Brown J. M., Janka H. T., 2016, ApJ, 821, 38
Sullivan M. et al., 2011, ApJ, 732, 118
Taddia F. et al., 2018, A&A, 609, A136
Tauris T. M., Langer N., Podsiadlowski P., 2015, MNRAS, 451, 2123
Tonry J. L. et al., 2018, PASP, 130, 064505
Tonry J. et al., 2021, Transient Name Server Discovery Report, 2021-360, 1
Tsujimoto T., Shigeyama T., 2001, ApJ, 561, L97
Vallely P. J., Kochanek C. S., Stanek K. Z., Fausnaugh M., Shappee B. J., 2021, MNRAS, 500, 5639
Waters C. Z. et al., 2020, ApJS, 251, 4
Waxman E., Katz B.,2017, in Alsabti A. W., Murdin P., eds, Handbook of Supernovae. Springer International Publishing, Cham, p. 967
Wellstein S., Langer N., 1999, A&A, 350, 148
Wellstein S., Langer N., Braun H., 2001, A&A, 369, 939
Wheeler J. C., Johnson V., Clocchiatti A., 2015, MNRAS, 450, 1295 (W15)
Williams R. E., 1987, ApJ, 320, L117
Woosley S. E., Langer N., Weaver T. A., 1995, ApJ, 448, 315
Xiang D. et al., 2019, ApJ, 871, 176
Yao Y. et al., 2020, ApJ, 900, 46
Yaron O., Gal-Yam A., 2012, PASP, 124, 668

SUPPORTING INFORMATION

Supplementary data are available at *MNRAS* online.

TableA1.csv
TableA2.txt
TableA3.txt

Please note: Oxford University Press is not responsible for the content or functionality of any supporting materials supplied by the authors. Any queries (other than missing material) should be directed to the corresponding author for the article.

APPENDIX A: PHOTOMETRY DATA TABLES

This section gives the photometry for SN 2021bxu in Table A1, photometry of the local sequence stars used to calibrate the Swope light curves in Table A2, and photometry of the host galaxy ESO 478-G 006 in Table A3.

Table A1. Photometry of SN 2021bxu.

MJD (d)	Apparent magnitude	Absolute magnitude	Filter	Telescope
59218.29	>22.29	–	w	Pan-STARRS
59245.12	>17.60	–	g	ASAS-SN
59245.26	>19.60	–	o	ATLAS
59251.06	17.17 ± 0.09	-17.16 ± 0.19	g	ASAS-SN
59251.29	17.222 ± 0.018	-17.11 ± 0.16	c	ATLAS
59252.03	17.462 ± 0.007	-16.86 ± 0.16	r	Swope
59252.03	17.599 ± 0.011	-16.71 ± 0.16	i	Swope
59252.04	17.315 ± 0.011	-17.03 ± 0.16	B	Swope
59252.04	17.371 ± 0.008	-16.96 ± 0.16	g	Swope
59252.04	17.372 ± 0.010	-16.95 ± 0.16	V	Swope
59252.05	17.29 ± 0.11	-17.04 ± 0.19	g	ASAS-SN
59253.03	17.689 ± 0.015	-16.63 ± 0.16	r	Swope
59253.03	17.615 ± 0.017	-16.71 ± 0.16	V	Swope
59253.03	17.672 ± 0.012	-16.66 ± 0.16	g	Swope
59253.03	17.838 ± 0.019	-16.51 ± 0.16	u	Swope
59253.04	17.657 ± 0.019	-16.68 ± 0.16	B	Swope
59253.83	18.03 ± 0.17	-16.3 ± 0.2	g	ASAS-SN

Note. All magnitudes are given in the AB system. This table is available in its entirety in a machine-readable form in the online journal. A portion is shown here for guidance regarding its form and content.

Table A2. Photometry of the local sequence stars.

RA (J2000)	δ (J2000)	u (mag)	g (mag)	r (mag)	i (mag)	B (mag)	V (mag)
32.386726	−23.520622	18.00 ± 0.04	15.592 ± 0.008	–	–	16.035 ± 0.010	15.115 ± 0.010
32.213863	−23.394035	16.20 ± 0.02	15.412 ± 0.008	15.157 ± 0.012	–	15.620 ± 0.012	15.267 ± 0.010
32.385872	−23.476055	18.77 ± 0.07	16.238 ± 0.006	15.203 ± 0.012	–	16.697 ± 0.012	15.720 ± 0.009
32.299397	−23.491762	16.92 ± 0.02	15.888 ± 0.007	15.498 ± 0.008	15.365 ± 0.005	16.152 ± 0.010	15.659 ± 0.009
32.245022	−23.485291	17.00 ± 0.03	15.969 ± 0.007	15.594 ± 0.008	15.465 ± 0.005	16.223 ± 0.010	15.743 ± 0.009
32.199989	−23.418266	17.87 ± 0.04	16.586 ± 0.006	16.047 ± 0.008	15.853 ± 0.005	16.905 ± 0.013	16.294 ± 0.010
32.345909	−23.366911	18.69 ± 0.07	17.580 ± 0.007	17.130 ± 0.011	17.012 ± 0.010	17.87 ± 0.02	17.315 ± 0.014
32.385616	−23.374666	–	18.673 ± 0.017	17.261 ± 0.011	15.899 ± 0.006	19.17 ± 0.05	18.02 ± 0.02
32.226913	−23.380148	–	18.568 ± 0.015	17.249 ± 0.011	16.204 ± 0.006	19.23 ± 0.06	17.91 ± 0.02
32.393101	−23.397284	18.62 ± 0.06	17.688 ± 0.008	17.266 ± 0.011	17.132 ± 0.011	17.92 ± 0.02	17.442 ± 0.015
32.283989	−23.457907	–	18.795 ± 0.018	17.449 ± 0.012	16.290 ± 0.006	19.36 ± 0.06	18.10 ± 0.02
32.393776	−23.471512	–	19.15 ± 0.03	17.874 ± 0.016	17.387 ± 0.013	19.56 ± 0.07	18.55 ± 0.04
32.342522	−23.359810	–	19.42 ± 0.03	18.034 ± 0.018	16.771 ± 0.008	19.79 ± 0.10	18.71 ± 0.04
32.308815	−23.504641	–	19.31 ± 0.03	18.14 ± 0.02	17.499 ± 0.015	19.88 ± 0.10	18.65 ± 0.04
32.287636	−23.507380	–	19.40 ± 0.03	18.46 ± 0.03	18.01 ± 0.02	19.92 ± 0.10	18.87 ± 0.05
32.300083	−23.356009	–	19.60 ± 0.04	18.39 ± 0.02	17.487 ± 0.015	20.48 ± 0.18	19.07 ± 0.06
32.279221	−23.437853	18.95 ± 0.11	18.96 ± 0.02	18.51 ± 0.03	18.29 ± 0.03	19.15 ± 0.05	18.70 ± 0.04
32.270084	−23.510548	19.74 ± 0.16	18.91 ± 0.02	18.66 ± 0.03	18.57 ± 0.04	19.09 ± 0.04	18.76 ± 0.04
32.232883	−23.362158	–	20.38 ± 0.09	19.30 ± 0.06	18.52 ± 0.04	–	19.87 ± 0.13
32.285130	−23.352280	–	19.73 ± 0.04	19.46 ± 0.07	19.12 ± 0.08	20.13 ± 0.13	19.61 ± 0.11
32.226944	−23.370340	–	19.91 ± 0.05	19.42 ± 0.06	19.17 ± 0.08	20.20 ± 0.13	19.71 ± 0.12
32.355373	−23.451790	–	20.10 ± 0.07	18.78 ± 0.03	18.24 ± 0.03	20.46 ± 0.17	19.13 ± 0.07
32.256466	−23.395746	–	–	19.39 ± 0.06	18.72 ± 0.05	–	–
32.336956	−23.473841	–	20.22 ± 0.07	19.09 ± 0.04	18.50 ± 0.04	–	19.64 ± 0.11
32.302109	−23.528551	–	20.86 ± 0.15	19.75 ± 0.09	18.43 ± 0.03	–	–
32.274239	−23.415289	–	20.78 ± 0.14	19.96 ± 0.13	18.40 ± 0.03	–	–
32.277119	−23.527414	–	–	19.67 ± 0.08	18.76 ± 0.05	–	–
32.338875	−23.392778	19.78 ± 0.17	19.59 ± 0.04	18.98 ± 0.04	18.65 ± 0.04	19.70 ± 0.08	19.25 ± 0.07
32.276211	−23.391331	14.494 ± 0.016	–	–	–	–	–
32.307014	−23.431122	16.41 ± 0.02	–	–	–	15.333 ± 0.012	–
32.352291	−23.418312	15.618 ± 0.018	–	–	–	14.742 ± 0.012	–
32.361607	−23.421463	15.777 ± 0.018	–	–	–	–	–

Note. All magnitudes are given in the natural Swope system. This table is available in its entirety in a machine-readable form in the online journal.

Table A3. Photometry of the host galaxy ESO 478- G 006.

Filter	Magnitude	Mag. Error
Swift *UVW*1	14.96	0.02
Swift *U*	14.19	0.01
PS *g*	13.05	0.01
PS *r*	12.63	0.01
PS *i*	12.34	0.01
PS *z*	12.11	0.01
PS *Y*	12.14	0.01
2MASS *J*	11.60	0.02
2MASS *H*	11.40	0.02
2MASS K_s	11.54	0.03
WISE *W*1	13.01	0.02
WISE *W*2	13.44	0.02

Note: All magnitudes are given in the AB system. This table is available in its entirety in a machine-readable form in the online journal.

[1]*Institute for Astronomy, University of Hawai'i at Mānoa, 2680 Woodlawn Drive, Honolulu, HI 96822, USA*
[2]*Department of Physics, Virginia Tech, Blacksburg, VA 24061, USA*
[3]*Las Campanas Observatory, Carnegie Observatories, Casilla 601, La Serena, Chile*
[4]*Institute of Space Sciences (ICE, CSIC), Campus UAB, Carrer de Can Magrans, s/n, E-08193 Barcelona, Spain*
[5]*Institut d'Estudis Espacials de Catalunya (IEEC), Gran Capità, 2-4, Edifici Nexus, Desp. 201, E-08034 Barcelona, Spain*
[6]*The Observatories of the Carnegie Institution for Science, 813 Santa Barbara St, Pasadena, CA 91101, USA*
[7]*Department of Physics, Florida State University, 77 Chieftan Way, Tallahassee, FL 32306, USA*
[8]*Space Telescope Science Institute, 3700 San Martin Drive, Baltimore, MD 21218, USA*
[9]*Department of Physics and Astronomy, Aarhus University, Ny Munkegade, DK-8000 Aarhus C, Denmark*
[10]*Homer L. Dodge Department of Physics and Astronomy, University of Oklahoma, 440 W. Brooks, Rm 100, Norman, OK 73019, USA*
[11]*Hamburger Sternwarte, Gojenbergsweg 112, D-21029 Hamburg, Germany*
[12]*Facultad de Ciencias Astronómicas y Geofísicas, Universidad Nacional de La Plata, Paseo del Bosque S/N, La Plata B1900FWA, Argentina*
[13]*Instituto de Astrofísica de La Plata (IALP), CCT-CONICET-UNLP, Paseo del Bosque S/N, La Plata B1900FWA, Argentina*
[14]*Kavli Institute for the Physics and Mathematics of the Universe (WPI), The University of Tokyo, 5-1-5 Kashiwanoha, Kashiwa, Chiba 277-8583, Japan*
[15]*Mitchell Institute for Fundamental Physics and Astronomy, Department of Physics and Astronomy, Texas A&M University 4242 TAMU, College Station, TX 77845, USA*
[16]*Astrophysics Research Institute, Liverpool John Moores University, IC2, Liverpool Science Park, 146 Brownlow Hill, Liverpool L3 5RF, UK*
[17]*European Southern Observatory, Alonso de Córdova 3107, Casilla 19, Santiago, Chile*
[18]*Millennium Institute of Astrophysics MAS, Nuncio Monsenor Sotero Sanz 100, Off. 104, Providencia, Santiago, Chile*
[19]*Technische Universität München, TUM School of Natural Sciences, Physik-Department, James-Franck-Straße 1, D-85748 Garching, Germany*
[20]*Max-Planck-Institut für Astrophysik, Karl-Schwarzschild Straße 1, D-85748 Garching, Germany*
[21]*Astrophysics Research Centre, School of Mathematics and Physics, Queen's University Belfast, Belfast BT7 1NN, UK*
[22]*Astronomical Observatory, University of Warsaw, Al. Ujazdowskie 4, PL-00-478 Warszawa, Poland*
[23]*Cardiff Hub for Astrophysics Research and Technology, School of Physics & Astronomy, Cardiff University, Queens Buildings, The Parade, Cardiff CF24 3AA, UK*
[24]*Istituto Nazionale di Astrofisica, Viale del Parco Mellini 84, I-00136 Rome, Italy*

This paper has been typeset from a TEX/LATEX file prepared by the author.